

Machine Learning Methods for Stellar Collisions. I. Predicting Outcomes of SPH Simulations

ELENA GONZÁLEZ PRIETO,^{1,2,3} JAMES C. LOMBARDI, JR.,⁴ SANAE A. C. ROSE,^{2,3} CHARLES F.A. GIBSON,^{1,2,3}
 CHRISTOPHER E. O'CONNOR,^{2,3} TJITSKE STARKENBURG,^{1,2,3} FULYA KIROĞLU,^{2,3} KYLE KREMER,⁵
 TRISTAN C. PARMERLEE,⁶ AND FREDERIC A. RASIO^{1,2,3}

¹Department of Physics & Astronomy, Northwestern University, Evanston, IL 60208, USA

²Center for Interdisciplinary Exploration & Research in Astrophysics (CIERA), Northwestern University, Evanston, IL 60201, USA

³NSF-Simons AI Institute for the Sky (SkAI), 172 E. Chestnut St., Chicago, IL 60611, USA

⁴Department of Physics, Allegheny College, Meadville, Pennsylvania 16335, USA

⁵Department of Astronomy & Astrophysics, University of California, San Diego; La Jolla, CA 92093, USA

⁶Department of Physics, Loyola University Chicago, Chicago, IL 60660, USA

ABSTRACT

Stellar collisions can occur frequently in dense cluster environments, and play a crucial role in producing exotic phenomena from blue stragglers in globular clusters to high-energy transients in galactic nuclei. Successive collisions and mergers of massive stars could also lead to the formation of massive black holes, serving as seeds for supermassive black hole in the early universe. While analytic fitting formulae exist for predicting collision outcomes, they do not generalize across different energy scales or stellar evolutionary phases. Smoothed particle hydrodynamics (SPH) simulations are often used to compute the outcomes of stellar collisions, but, even at low resolution, their computational cost makes running on-the-fly calculations during an N -body simulation quite challenging. Here we present a new grid of 27,720 SPH calculations of main-sequence star collisions, spanning a wide range of masses, ages, relative velocities, and impact parameters. Using this grid, we train machine learning models to predict both collision outcomes (merger vs disruption, or flyby) and final remnant masses. We compare the performance of nearest neighbors, support vector machines, and neural networks, achieving classification balanced accuracy of 98.4%, and regression relative errors as low as 0.11% and 0.15% for the final stars 1 and 2, respectively. We make our trained models publicly available as part of the package `collAIder`, enabling rapid predictions of stellar collision outcomes in N -body models of dense star cluster dynamics.

1. INTRODUCTION

Stellar collisions and mergers are important across a wide range of dense stellar systems, from galactic nuclei to open clusters (Spitzer & Saslaw 1966; Sanders 1970; Lombardi et al. 1996; Hurley et al. 2001; Shara 2002; Hurley et al. 2005; Glebbeek et al. 2008; Dale et al. 2009; Balberg & Yassur 2023; González Prieto et al. 2024). The properties and outcomes of these collisions vary drastically depending on the environment. In galactic nuclei, stars collide at relative velocities of hundreds to thousands of kilometers per second (e.g., Rauch 1999; Genzel et al. 2010; Rose et al. 2023), while in globular clusters, typical velocity dispersions are only tens of kilometers per second (e.g., Pryor & Meylan 1993; Harris 2010; Baumgardt & Hilker 2018). Whether a collision results in a merger, mass stripping, or complete disruption depends on this relative velocity, as well as the pericenter distance, and the mass, radius, and evolutionary stage of each star (e.g., Freitag & Benz 2005).

Understanding how these dynamical parameters shape collision outcomes has proven crucial to explain exotic stellar objects and phenomena. For example, blue stragglers, stars that appear on the main sequence (MS) beyond the turnoff, could be formed through collisions between lower-mass MS stars (e.g., Leonard 1989; Lombardi et al. 1996; Sills et al. 2009). Stellar collisions have also been studied for their possible role as gravitational-wave progenitors (e.g., Kiroğlu et al. 2025; González Prieto et al. 2024; Amaro Seoane 2023; Kremer et al. 2020; Gürkan et al. 2006; Portegies Zwart et al. 2004). Transient events are also expected, such as tidal disruption events (TDE) (e.g., Perets et al. 2016; Kremer et al. 2019; Lopez et al. 2019; Wang et al. 2021; Kremer et al. 2022; Ryu et al. 2022; Kiroğlu et al. 2023; Xin et al. 2024; Ryu et al. 2024; Rose & Mockler 2025), energetic explosions from collisions between hypervelocity stars in galactic nuclei (Hu & Loeb 2024; Brutman et al. 2024; Balberg et al. 2013), and collision-driven events (van der Merwe et al. 2024, 2025; Peng et al. 2025). Furthermore, high-speed collisions between intermediate-mass stars can produce stripped stellar remnants (e.g., Rose et al. 2023; Freitag et al. 2007; Rauch 1999; Lai et al. 1993) with abundance ratios similar to those observed in the TDE ASASSN-14ko (e.g., Payne et al. 2021; Gibson et al. 2024). Lastly, mergers can also produce exotic

signatures, such as gamma-ray production from a black hole merger with a helium star (e.g., O’Connor et al. 2025; Neights et al. 2026) or luminous red novae (e.g., Kirilov et al. 2025; Metzger & Pejcha 2017; MacLeod et al. 2017; Ivanova et al. 2013).

Currently, most N -body models of dense stellar systems have simplified treatments for stellar collisions, such as the “sticky sphere” approximation where no mass is lost during the collision. While this assumption is adequate for nearly parabolic collisions in globular clusters, hyperbolic collisions in nuclear star clusters can produce significant shock-driven mass loss. Accurately predicting the detailed outcomes of stellar collisions, such as remnant masses and structures, therefore requires 3D hydrodynamics simulations that can resolve relevant thermodynamical and hydrodynamic processes, using methods such as smooth particle hydrodynamics (SPH) (Rasio 1991; Monaghan 1992; Gaburov et al. 2010) or grid-based/moving-mesh methods (Weinberger et al. 2020). However, these detailed simulations are computationally expensive, sometimes requiring days of wallclock time per collision, making on-the-fly calculations in N -body cluster simulations infeasible. As a result, a practical approach is to precompute large grids of SPH results and develop fitting formulae (e.g., Rose et al. 2025; Lai et al. 1993; Rauch 1999).

Machine learning (ML) offers a unique opportunity to overcome these computational limitations. Using traditional ML algorithms, a model can be trained on a large grid of simulations to learn the mapping between inputs and outputs. This approach has been proven effective in the context of planetary collisions. For example, Cambioni et al. (2019) compare classification and regression performance across multiple algorithms. This work was extended to predict core mass-fractions (Cambioni et al. 2021) and orbital parameters (Emsenhuber et al. 2020). Recently, Amaro Seoane (2025) and Rose et al. (2025) have applied similar techniques in the context of stellar collisions, with the former using an older grid of stellar collision SPH simulations presented in Freitag & Benz (2005) and the latter using a new grid of equal-mass but higher-resolution collision calculations.

For this study, we compute a comprehensive new grid of SPH results for stellar collisions, spanning wide ranges of ages, stellar masses, pericenter distances, and relative velocities. We improve upon the SPH simulations presented in Freitag & Benz (2005) by using accurate MESA stellar profiles and exploring the effects of stellar age on collision outcomes. Following the methodology of Cambioni et al. (2019), we compare the performance of multiple ML algorithms on both classification and regression tasks. The classification task predicts the number of surviving stars, while the regression task estimates their final masses. Furthermore, we compare different ML methods, including nearest neighbors (Cover & Hart 1967), support vector machines (Cortes & Vap-

nik 1995), and neural networks (e.g., McCulloch & Pitts 1943; Hornik et al. 1989; LeCun et al. 2015).

In Section 2, we describe our SPH simulations, including the MESA stellar models used as initial conditions. In Sections 3 and 4 we present our ML framework for classifying stellar collision outcomes and predicting the properties of final remnants. In Section 5 we compare these models against a Mixture of Experts architecture. We then introduce `collAIder` (in Sec. 6), a new software that leverages the trained ML models to make rapid predictions for stellar outcomes. Finally, in Section 7 we evaluate model performance on interpolated and extrapolated data. We summarize our results and outline future applications in Section 8.

2. METHODS

2.1. *Simulation Grid*

Our training set of SPH results is built by sampling across five parameters: the age of the system (t), the primary mass (M_1), the secondary mass (M_2), the velocity at infinity (v_∞), and the distance of closest approach (pericenter distance, r_p). Consistent with assumptions made in many star cluster modeling codes, we assume that all stars are coeval. However, we account for the mass-dependent timescale for stars to contract onto the MS, and we collide only MS stars. For example, at an age of 1 Myr, we only perform collisions involving the most massive stars in the grid, since stars below $4M_\odot$ are still in the pre-MS stage. Furthermore, some of the lower-mass stars will not reach the zero-age MS (ZAMS) before the higher-mass stars evolve off the MS. As a result, we do not compute collisions between the highest and lowest sampled masses. We restrict this initial grid to stars only on the MS because stellar structure varies greatly across the full age range of the sampled stellar masses. Accurately modeling the evolution of a wider range of collision outcomes across time would require a very finely-sampled grid of pre-MS, MS, and giant star encounters, an undertaking which we reserve for future work.

For the base grid, ages are sampled logarithmically in Gyr at $(-3, -2.5, -2, -1.5, -1, -0.5, 0, 0.5, 1)$ and at 13.7 Gyr (Hubble time). Stellar masses are sampled at ten values from 0.2 to $64M_\odot$. Velocities sampled are $(10, 100, 250, 500, 1000, 2000, 4000, 8000, 16000)$ km/s, chosen to span speeds typical of stellar collisions from globular clusters to galactic nuclei. Pericenter distances are sampled based on fractional enclosed mass f : for each collision we choose f (uniformly in steps of 0.1 from 0 to 0.9, with additional samples at 0.95, 0.97, 0.99, and 1), compute the radii $r_1(f)$ and $r_2(f)$ that enclose this mass fraction in each parent star, and set the pericenter to $r_p = r_1(f) + r_2(f)$. For example, $f = 0$ corresponds to a head-on collision and $f = 1$ to a grazing encounter at the sum of the two stellar radii.

We complement the base grid by sampling the terminal age main sequence (TAMS) for all stellar masses,

defined as the point when the central hydrogen mass fraction drops below 10^{-5} . We also compute a grid at the ZAMS age for the 64, 32, 16, 8, and $4M_{\odot}$ stars, where ZAMS is defined as the local minimum in luminosity when nuclear burning provides more than 50% of the luminosity. For the ZAMS grid, each star at the ZAMS is collided with all other stars that are on the MS at that time, but we do not simulate collisions among the MS stars at that time. This brings the total grid size to 27,720 SPH simulations of stellar collisions. The complete grid is shown in Figure 1, where the lower right panel illustrates how each mass and time slice is sampled in r_p and v_{∞} .

2.2. Stellar Profiles

To generate the realistic stellar profiles needed for the stellar collision simulations, we use **MESA** (v24.08.1) (Paxton et al. 2011, 2013, 2015, 2018, 2019; Jermyn et al. 2023). We scale the initial chemical composition of our stellar models relative to the proto-solar helium abundance $Y_{\odot} = 0.2703$ and metallicity $Z_{\odot} = 0.0142$ of Asplund et al. (2009). We adopt a metallicity of $Z = 0.01Z_{\odot}$ and calculate the corresponding helium abundance using equation 2 in Choi et al. (2016) (assuming $Y_p = 0.249$ from Planck Collaboration et al. (2016)), yielding a value of $Y = 0.249$. We treat microphysical processes relevant to MS stars following the Posydon model grids (Fragos et al. 2023; Andrews et al. 2025) unless otherwise specified. All **MESA** inlists used to generate our stellar models are available for download ¹.

We do not include stellar winds or rotation since we only perform collisions for stars on the MS. At this metallicity and evolutionary stage, mass loss is not expected to be very efficient. Future grids with stars past the MS will incorporate stellar rotation and metallicity-dependent wind prescriptions.

2.3. Smoothed Particle Hydrodynamics

The stellar collisions are performed using **StarSmasher** (Rasio 1991; Gaburov et al. 2010), a Lagrangian SPH code in which each fluid particle is assigned a mass, position, velocity, and specific internal energy. The particles are evolved using a variational SPH formulation, with gravitational forces and energies computed using direct summation on NVIDIA GPUs (Gaburov et al. 2010). We neglect radiative cooling and heating. Each particle has an extended density profile described by a Wendland C4 kernel (Wendland 1995) with a compact support $2h_i$ (where h_i is the smoothing length of the particle). Artificial viscosity is computed as in Hwang et al. (2015).

Because all parent stars are on the MS, an analytic equation of state including ideal-gas and radiation pressure is employed. Radiation pressure can contribute ap-

preciablely in our high-mass models and may also become more important in shock-heated regions during the collision. For each SPH particle, given its density ρ , specific internal energy u , and mean molecular mass μ (with dimensions of mass), we obtain the temperature T by solving $u = \frac{3}{2}kT/\mu + aT^4/\rho$, where k is Boltzmann's constant and a is the radiation constant. The resulting quartic equation in T is solved analytically following Lombardi et al. (2006). We then compute the pressure from $P = \rho kT/\mu + \frac{1}{3}aT^4$.

Each star is composed of 10,000 particles with ~ 50 neighbors, where the 1D **MESA** stellar profiles are converted into 3D SPH models by placing particles in a stretchy hexagonal close-packed (HCP) lattice as described in Appendix A of Gibson et al. (2024). The value of **equalmass** is set to 0.5 for most models, yielding unequal mass particles with a number density $n \propto \sqrt{\rho}$ to distribute more particles closer to the center of the star and better resolve the core. After constructing the stellar profile, the particles are relaxed into hydrostatic equilibrium as described in Lombardi et al. (2006) and Gaburov et al. (2010).

For later post-processing, we store snapshots of the system at an output interval roughly equal to the dynamical timescale of the more massive star: $\Delta t_{\text{out}} \equiv t_{\text{dyn}} = \sqrt{R_{\text{max}}^3/(GM_{\text{max}})} = \sqrt{M_{\text{max}}}$ in code units ($G = M_{\odot} = R_{\odot} = 1$), where for the purposes of assigning a Δt_{out} value, we have adopted the approximate mass-radius relation $R/R_{\odot} = (M/M_{\odot})^{2/3}$. Here, R_{max} and M_{max} are, respectively, the radius R and mass M of the more massive of the two parent stars. We compute the bound mass of each star at every snapshot using an iterative energy-based procedure similar to that of Lombardi et al. (2006). At a given snapshot, we first compute the center-of-mass (COM) and preliminary mass of each stellar component. Then, we evaluate each SPH particle's specific mechanical energy with respect to each star's COM.

This mechanical energy includes only kinetic and gravitational potential terms, as recommended by Nandez et al. (2014). A particle is considered gravitationally bound to star j if its mechanical energy relative to that star's COM is negative. In particular, for particle i relative to component j , we require $v_{ij}^2/2 - G(M_j - m_i)/d_{ij} < 0$, where v_{ij} is the particle's speed in the frame of star j 's COM, d_{ij} is its distance from that center, m_i is the mass of the particle, and M_j is the current mass of star j . This approach is equivalent to using the Bernoulli equation at late times, since internal energy and enthalpy become negligible in the outflow after sufficient adiabatic expansion. To avoid spuriously identifying poorly resolved clumps as stars, a bound component is considered a stellar remnant only if it contains at least 20 SPH particles. Otherwise, its particles are reassigned to the unbound mass.

We iterate this procedure to refine the bound masses self-consistently. Based on its assignment from the pre-

¹ Will be made available at time of publication.

vious snapshot (or the known configuration at $t = 0$), each particle is tentatively assigned to the component (star 1 or star 2) for which it has negative energy, or to the unbound mass otherwise. If it has a negative mechanical energy with respect to both stars, it is assigned to whichever star yields the most negative energy. We then update the COM and mass of each star based on these assignments and recompute the energies, repeating until no particle changes its affiliation (typically converging within a few iterations). Particles that do not have negative mechanical energy with respect to either star are assigned to the unbound component.

The stopping time (t_f) is dynamically determined by evaluating the state of the system once per output interval Δt_{out} . At each interval, **StarSmasher** identifies the current bound components and then computes their orbital elements. If a merger is detected (i.e., the number of bound components decreases), or if a binary remains bound, we extend the run by resetting $t_f = \max(t_f, t + 30 \Delta t_{\text{out}})$, where t is the current time, ensuring at least 30 additional outputs. Whenever t_f is updated, the total internal energy is stored, and if it later changes by more than 1% the run is again extended by $30 \Delta t_{\text{out}}$ to avoid stopping during ongoing thermal readjustment. In cases for which fewer than 100 particles remain in a remnant, we enforce a minimum integration time by setting $t_f = \max(t_f, 100 \Delta t_{\text{out}})$ to ensure that the remnant is long-lived. The simulation ends when the time reaches $t = t_f$.

3. CLASSIFICATION OF COLLISION OUTCOMES

The first quantity we aim to predict is the qualitative outcome of the collision, closely related to the number of stars remaining after the encounter. In terms of survivors, there are three possibilities: 0, 1, or 2 stars. At sufficiently large pericenter distances, collisions are grazing enough that both stars survive, though not completely intact. As the pericenter distance decreases and collisions become more head-on, the outcome depends more strongly on the relative velocity of the objects, their mass ratio, and details of their stellar structures. For any two colliding stars at sufficiently low relative velocities, the collision will result in a merger. However, as the relative velocity increases at small pericenter distances, collisions can become energetic enough to unbind the material from both stars, leaving no remnants.

A special scenario arises in the unequal-mass collisions where, at high enough velocities and moderately off-axis trajectories, only one star is destroyed while the other survives. This results in the surviving star being stripped of its envelope, and so we will refer to these cases as the “stripping” scenario. Although the same number of stars remain as in the merger case, we designate this as a separate class because the underlying hydrodynamic evolution and the properties of the final remnant are qualitatively different.

To distinguish between merger and stripped-star outcomes, we monitor the relative orbit and proximity of the two stellar components throughout the collision. In the post-processing, a merger occurs when two star components become gravitationally bound in such a tight encounter that the semimajor axis of their orbit falls below a critical threshold related to their tidal radii and sizes. Specifically, the code estimates each star’s tidal disruption radius as $r_{\text{tidal},i} = R_i (M_j/M_i)^{1/3}$, with $j \neq i$ and with the effective radius of component i estimated as $R_i = (I_i/M_i)^{1/2}$. Here, I_i is the moment of inertia about the rotation axis, M_i is the total bound mass of component i , and M_j is the total bound mass of the other component (that is, $j = 2$ if $i = 1$, while $j = 1$ if $i = 2$). If the semimajor axis is smaller than $\min(r_{\text{tidal},i}, R_j)$ for either component, then we consider this a merger and immediately combine the bound particle sets of the two stars. In the case of no mergers and one star remaining, then we classify the remaining star as a stripped star.

We therefore define a four-class classification task with labels 0, 1, 2, 3, where classes 0, 1, and 2 indicate the number of surviving stars, and class 3 represents the case where a stripped star survives (as opposed to a merger). Before training a model on the simulation data, we transform the input parameters to ensure that they all span comparable ranges, facilitating model training. We apply variable-specific transformations to each component of the five-dimensional input space that account for their dynamics ranges:

$$\{\log(t+0.001), \log(r_p+0.1), \log(v_\infty+10), \ln(M_1), \ln(M_2)\} \quad (1)$$

where t is in units of Gyr, r_p in solar radii, v_∞ in km/s and the stellar masses in solar masses. To avoid singularities near zero, we introduce offsets for T , r_p , and v_∞ with the same units and scales as the corresponding variables.

In the context of stellar collisions, the pericenter distance is often normalized by the stellar radii to obtain a dimensionless parameter. However, this introduces a strong sensitivity to errors in the stellar radius estimates, which are known to be significant in some cases—for example, for massive stars in the Single Star Evolution (SSE) code (see Figure 8 in [Agrawal et al. 2020](#)). To avoid this issue, we train our ML model using pericenter distances in units of solar radii. Consequently, the pericenter values that the model is trained on vary in scale depending on the stellar masses involved.

Additionally, all methods presented below normalize the data following

$$x'_i = \frac{x_i - \mu_i}{\sigma_i}. \quad (2)$$

where μ_i and σ_i are the mean and standard deviation of input parameter i , respectively.

The dataset is divided into 70% training, 15% validation, and 15% testing, corresponding to 19404, 4158, and

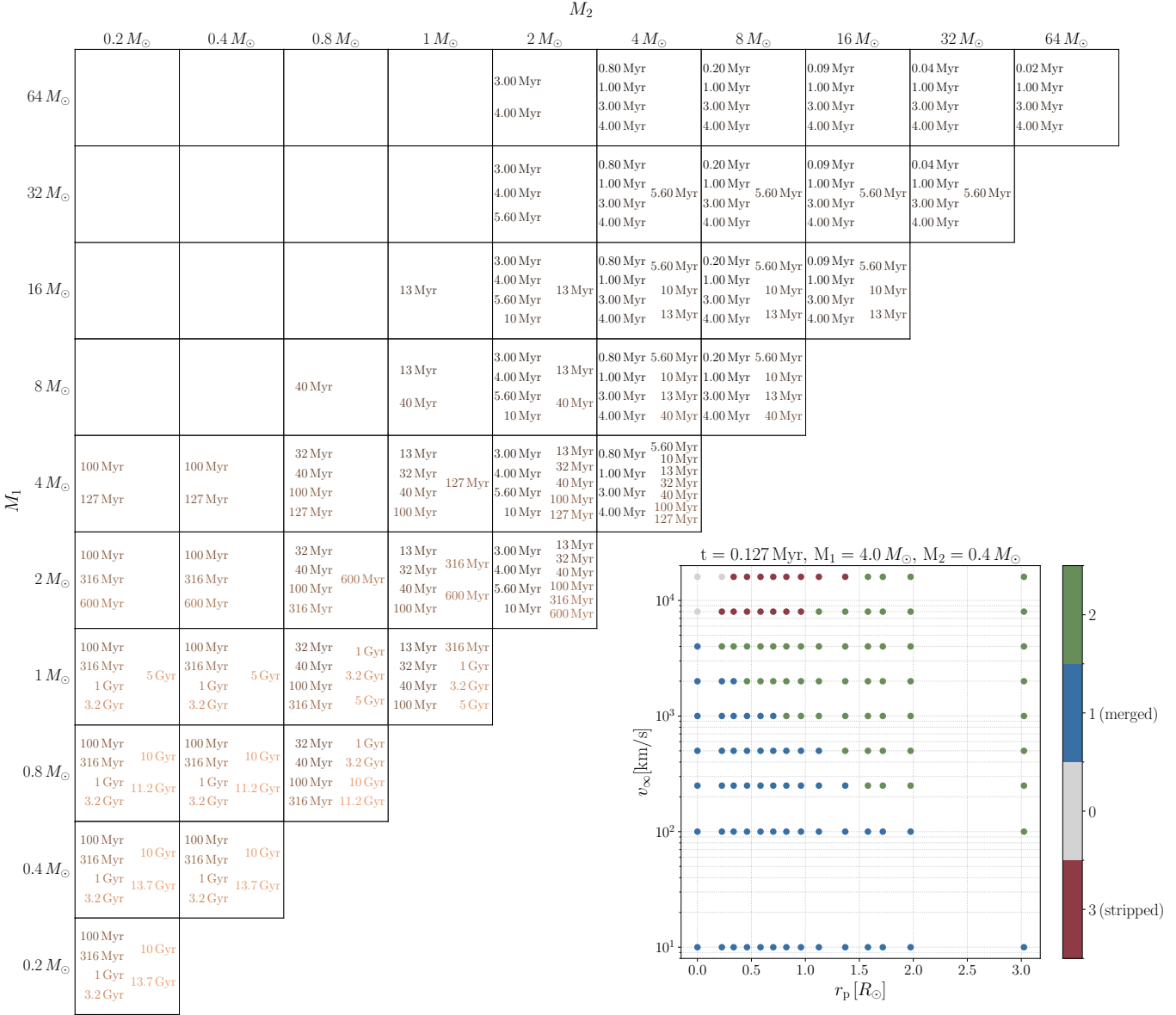


Figure 1. Complete grid of SPH stellar collision simulations. The left and top axes show the primary and secondary masses in the collisions, respectively. Within each square, the corresponding times at which the collisions were sampled are shown, colored to indicate different times. In the lower right corner, we show an example of how the pericenter distance (r_p) and velocity at infinity (v_∞) are sampled at each age, M_1 , and M_2 dimensions. The colors illustrate the number of stellar remnants, where we distinguish cases where the stars merge from those that result in a stripped star.

4158 samples. Through stratified sampling, we ensure that each split preserves the overall label proportions. There exists a class imbalance for the stripping (label 3) and mutually destructive cases (label 0). For instance, in the training dataset, they each represent only 4.8% and 8.1% of the samples, respectively. We prioritize models that optimize predictions across all classes, not just the overrepresented ones. Below, we will present three algorithms used for the classification task, and discuss how they compare to each other.

3.1. *k*-Nearest Neighbors

k-Nearest Neighbors (*k*-NN) (Cover & Hart 1967) is a well-established ML algorithm that classifies data points based on the labels of their “*k*” closest neighbors. The number of neighbors considered, distance metric, and weighting scheme are all hyperparameters that can be tuned to optimize model performance. We perform a grid search over the number of neighbors (between 3 and 25), the distance metric (Euclidean or Manhattan), and weighting scheme (uniform for all points or weighted by inverse distance). Performance is evaluated using

balanced accuracy, which averages over the accuracies from each class and reduces sensitivity to class imbalance. The set of hyperparameters that yields the highest performance consists of five neighbors, Euclidean distance, and a weighting scheme in which points are weighted inversely proportional to their distance. The model achieves a test balanced accuracy of 91.7%, with both accuracy and balanced accuracy reported in Table 2, alongside the performance for the ML methods described below.

3.2. Support Vector Machines

Support Vector Machines (SVMs) (Cortes & Vapnik 1995) are supervised ML algorithms that optimize decision boundaries by finding hyperplanes that best separate the different classes in kernel space. Through kernel transformations, SVMs can classify non-linear data, making them particularly effective for complex datasets and multi-class classification.

As in the previous section, we perform a grid search to find the best-performing set of hyperparameters using the Support Vector Classifier (SVC) available in `scikit-learn` (Pedregosa et al. 2011). The relevant parameters to optimize with SVCs and the values we explore include (1) the kernel that transforms the input data into a higher-dimensional feature space (Gaussian radial basis function (`rbf`) or polynomial), (2) `C`, a regularizer that controls the complexity of the decision boundaries (0.1, 1, 10, 100, 1000, 10000), and (3) `gamma`, which controls how much influence a single data point has (0.001, 0.01, 0.1, 1). Within the polynomial kernel function, we also search over varying degrees (2 and 3).

As expected, we find `rbf` to be the optimal kernel, as it offers greater flexibility in non-linear decision boundaries. Furthermore, the best-performing hyperparameters are `C=10,000` and `gamma= 0.1`, yielding a test balanced accuracy of 97.7%. Since the optimized value of `C` is at the edge of the parameter search range, we perform an additional localized search with higher values, which still yields an optimized value of `C=10,000`.

3.3. Neural Network

Neural Networks (NNs) learn a mapping between inputs and outputs through a series of weighted transformations and non-linear activation functions (e.g., McCulloch & Pitts 1943; LeCun et al. 2015). Our NN is a multi-layer perceptron (MLP) (Hornik et al. 1989) composed of three hidden layers, with 512, 256, and 128 neurons, respectively. Each hidden layer is followed by a Rectified Linear Unit (ReLU) activation function (e.g., Fukushima 1969; Glorot et al. 2011; Maas et al. 2013; Agarap 2018) and layer normalization (Lei Ba et al. 2016).

All hyperparameters, including network architecture, batch size, optimizer, initial learning rate, and scheduler parameters, were optimized through a hyperparam-

Table 1. Classification Hyperparameters

Parameter	Optimized Value	Search Range
Batch Size	64	64 – 256
Epochs	500	500 – 2000
Optimizer	AdamW	AdamW, sgd
Scheduler	CA-LR	CA-LR, RLRP
Learning Rate	0.0002	$10^{-5} – 0.1$
<code>patience</code>	...	10 – 60
<code>factor</code>	...	0.3 – 0.5

NOTE—Hyperparameter optimization search for the classification task. Acronyms: stochastic gradient descent (`sgd`), AdamW optimizer (`AdamW`), Cosine Annealing Learning Rate scheduler (`CA-LR`), and Reduce Learning Rate on Plateau scheduler (`RLRP`).

eter search using the Weights and Biases platform². We performed a Bayesian optimization (Snoek et al. 2012) sweep, which efficiently identifies hyperparameter combinations that improve model performance based on previous attempts. Table 1 lists the ranges explored for each hyperparameter and its optimized value.

The training and validation data are split into batches of size 64. We use the AdamW (Loshchilov & Hutter 2017) optimizer with a weighted cross entropy loss function, where class weights account for the imbalanced representation of collision outcomes. The learning rate is dynamically adjusted using a `CosineAnnealingLR` scheduler, a feature available in the PyTorch library (Paszke et al. 2019). The learning rate starts at 0.0002 and decreases following a cosine function down to a minimum value of 10^{-8} . The model is trained for 500 epochs, which we find sufficient for convergence. The `patience` and `factor` parameters belong to the `ReduceLROnPlateau` scheduler, where the learning rate decreases by a factor if a target metric (in our case the validation balanced accuracy) does not improve for a certain number of consecutive epochs (determined by the `patience` parameter). No optimized values for these two hyperparameters are shown, since the best performing model uses a `CosineAnnealingLR` scheduler.

For each training run, the epoch with the highest validation balanced accuracy is saved. Among the models in the hyperparameter optimization sweep, the one with the highest validation balanced accuracy was chosen. Its stability was then assessed by performing an additional sweep across ten different random seeds. The mean and standard deviation of the test accuracy and balanced accuracy across these ten runs are reported in Table 2. We do not perform this stability test for the other methods because k -NN is a non-parametric

² <https://wandb.ai/site/>

Table 2. Classification Performance

Method	Accuracy [%]	Balanced Accuracy [%]
k -NN	96.0	91.7
SVC	98.3	97.7
NN	98.5 ± 0.4 (Best: 98.6)	97.9 ± 0.2 (Best: 98.4)

NOTE—Performance on the classification task across different methods. For the neural network (NN), we report mean and standard deviation across ten runs with optimized hyperparameters and different random seeds. The best performing run (shown in parentheses) is used in subsequent figures.

method and SVC finds a global solution, unlike neural networks where random weight initialization can lead to different model performance. The best-performing model from this sweep is used in all subsequent analyses, and achieves a balanced accuracy of 98.4%.

3.4. Algorithm Performance Comparisons

Table 2 lists the testing accuracies and balanced accuracies across the three methods. The SVC and NN achieve comparable performances, both outperforming k -NN, our baseline. The SVC’s competitive performance is expected, as it explicitly maximizes the margin to the decision boundary, which proves effective for our dataset.

Figure 2 shows the confusion matrix for each method, summarizing classification performance across the class labels. High values along the diagonal indicate optimal performance, which correspond to correct predictions for each class. Both the SVC and NN outperform k -NN, our baseline, across all classes. k -NN and SVC perform best in the classes with larger number of training samples and struggle with undersampled cases, particularly scenarios where no stars survive (class 0) or where one stripped star remains after a destructive collision at high relative velocity (class 3). For both methods, class 3 exhibits the lowest accuracy. The reduced performance for class 3 can be attributed to a combination of two factors: (1) its limited number of samples and (2) its strong dependence on stellar structure. In particular, the location and extent of the region where this outcome occurs vary significantly across evolutionary times and mass ratios. For example, as illustrated later in Figure 3, the region of class 3 outcomes when the $32M_{\odot}$ star is at the TAMS stage (rightmost panel) occurs at lower pericenter distances than at an earlier time (middle panel), and is not present in the equal mass collision (leftmost panel).

The NN has more balanced performance, in part due to the use of a weighted cross entropy loss function that penalizes misclassifications in class 3 more heavily. As a result, the NN outperforms the SVC on minority classes.

For both methods, the most common misclassifications occur when samples from label 2 (a majority class) are classified as label 3 (a minority class). This is also likely due to the chosen optimization strategy, which prioritizes performance on minority classes and consequently leads to an increased number of misclassifications in the majority classes.

To visualize how these methods differ in their classification strategies, we show example decision boundaries in feature space in Figure 3. Each row showcases the predictions from the different ML algorithms while each column represents different physical scenarios.

The first column shows collision outcomes for an equal-mass interaction as a function of normalized pericenter distance and relative velocity at infinity. For visualization purposes, the pericenter distance has been normalized with respect to the sum of the stellar radii; however, the models were trained using the unnormalized pericenter values. Model predictions are shown as a shaded background, while the ground-truth labels are indicated by the colors of the data points. The middle column illustrates a collision between unequal-mass stars with a mass ratio of ~ 0.13 . The rightmost column shows collision outcomes when the primary star, in this case a $32M_{\odot}$ star, is on the TAMS.

Because the pericenter distance is sampled across radii enclosing a fixed mass fraction, the pericenter distances at the TAMS are smaller than at earlier evolutionary stages. This reflects the structural evolution of the $32M_{\odot}$ star, which develops a steeper density profile as it approaches the TAMS. Consequently, the third column highlights the sensitivity of the collision outcome to stellar structure, as the stripping class occurs at smaller relative pericenter distances compared to the earlier evolutionary stages.

Across each column, we show 2D projections of the decision boundaries produced by each algorithm. The k -NN method does not predict smooth decision boundaries, but rather has artificial features due to the intrinsic distances between the sampled neighbors. In contrast, the SVC produces smoother decision boundaries by finding hyperplanes that optimize the classification performance in kernel space. However, discontinuities appear at small pericenter distances, which are likely artifacts of projecting a higher-dimensional decision surface onto two dimensions and suggest that the SVC may produce overly complex decision surfaces that introduce nonphysical features.

Despite the comparable test balanced accuracies for the SVC and NN, the smoothest and most physically-consistent decision boundaries are achieved with the NN. This reflects the NN’s ability to learn complex, non-linear mappings between inputs and outputs, enabling it to capture the dependencies across features and therefore produce more physically-consistent classification predictions. In contrast, SVCs are optimized to find hyperplanes that separate classes using support

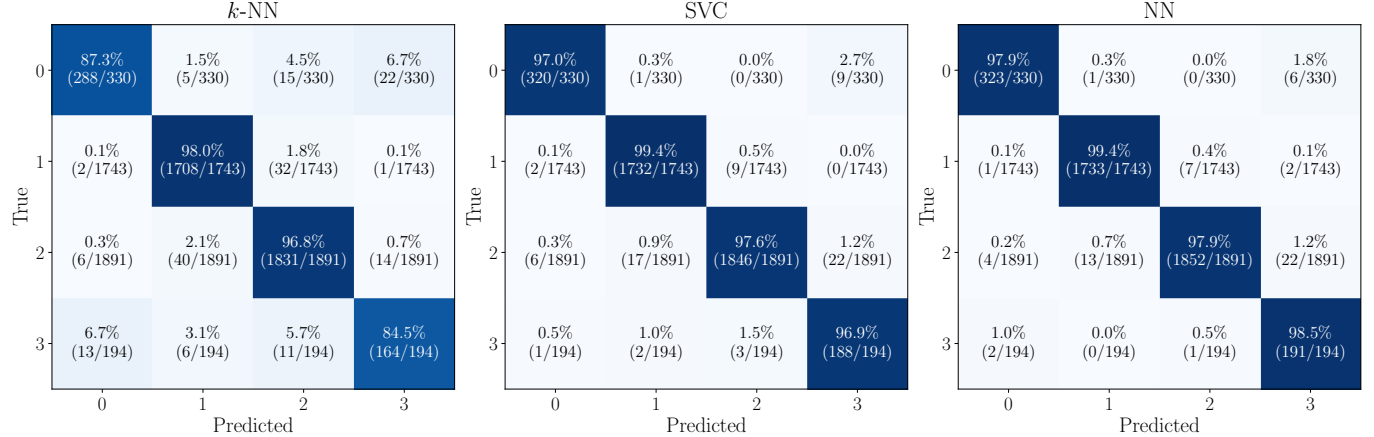


Figure 2. From left to right, confusion matrices for the testing data using k-Nearest Neighbors algorithm (*k*-NN), Support Vector Classifier (SVC), and a Neural Network (NN). The accuracy and total number of samples in each class are shown.

vectors and therefore struggle in areas where data may be sparse or classes are imbalanced.

As expected, most misclassifications occur near the decision boundaries, where small changes in pericenter distance or velocity can yield different outcomes. The boundaries shift with stellar mass and age, highlighting the complexity of the classification task. Nevertheless, despite a high-dimensional dataset that encompasses a wide range in its feature space, both the SVC and NN achieve remarkable accuracies. In future work, we will incorporate active learning to guide the optimal way to expand the dataset and further improve model performance.

4. REGRESSION OF COLLISION OUTCOME PROPERTIES

An additional set of key quantities to predict are the final properties of stellar collision remnants, particularly their final masses. This is motivated in part by the fact that most *N*-body codes—especially those modeling environments with low velocity dispersions—assume no mass loss during stellar mergers (the “sticky sphere approximation”). However, this assumption can break down at small pericenter distances and higher velocities.

To predict the final masses of the colliding stars (or the merger product, if the stars merge), we again compare three methods: *k*-NN, SVM, and NN. Rather than directly predicting the final masses, we predict three normalized mass fractions:

$$\left\{ \frac{M_{1,f}}{M_{\text{tot},i}}, \frac{M_{2,f}}{M_{\text{tot},i}}, \frac{M_{u,f}}{M_{\text{tot},i}} \right\} \quad (3)$$

where $M_{1,f}$ and $M_{2,f}$ are the final masses of stars 1 and 2, respectively, $M_{\text{tot},i}$ is the total initial mass of the system, and $M_{u,f}$ is the final unbound mass.

By construction, these three mass fractions always sum to unity due to mass conservation. Formatting the regression targets in this way encourages our models to predict physically consistent mass estimates. To reduce

inhomogeneities in the dataset without altering the outcome of the collisions, we assign the final merger product mass to star 1 in the case of a single remnant. The same input data is used as in Section 3, and results are summarized in Table 4.

4.1. *k*-Nearest Neighbors

To perform regression using the *k*-NN method, we conduct the same search strategy as in Section 3.1, but score models using the mean absolute error (MAE). Because the regression targets are mass fractions, the MAE is relative to the initial total mass in the system. To evaluate model performance on the test dataset, we multiply the predicted fractions by $M_{\text{tot},i}$ and compute the absolute errors in the final masses, as well as relative errors for cases in which the star survives. The optimized *k*-NN model uses 3 neighbors, Euclidean metric, and a inverse-distance weighting. The resulting median absolute errors in $M_{1,f}$ and $M_{2,f}$ are $0.021M_{\odot}$ and $1e-05M_{\odot}$, respectively.

4.2. Support Vector Regression

To perform regression with an SVM, we use Epsilon-Support Vector Regression (SVR hereafter). The algorithm learns a regression hyperplane, where ϵ defines the margin around the hyperplane. Training points within the margins don’t contribute to the loss, while points outside the margins become support vectors that shape and optimize the hyperplane. Hyperparameter optimization is performed for each regression quantity separately, beginning with a coarse grid search and subsequently refining it. Full details of the hyperparameter search are outlined in Appendix A. The optimal configuration for all regression targets uses an `rbf` kernel with $C = 1$, $\epsilon = 0.00001$, and $\gamma = 10$. The resulting best model achieves median absolute errors in $M_{1,f}$ and $M_{2,f}$ of $0.028M_{\odot}$ and $0.021M_{\odot}$, respectively; additional performance metrics are listed in Table 4.

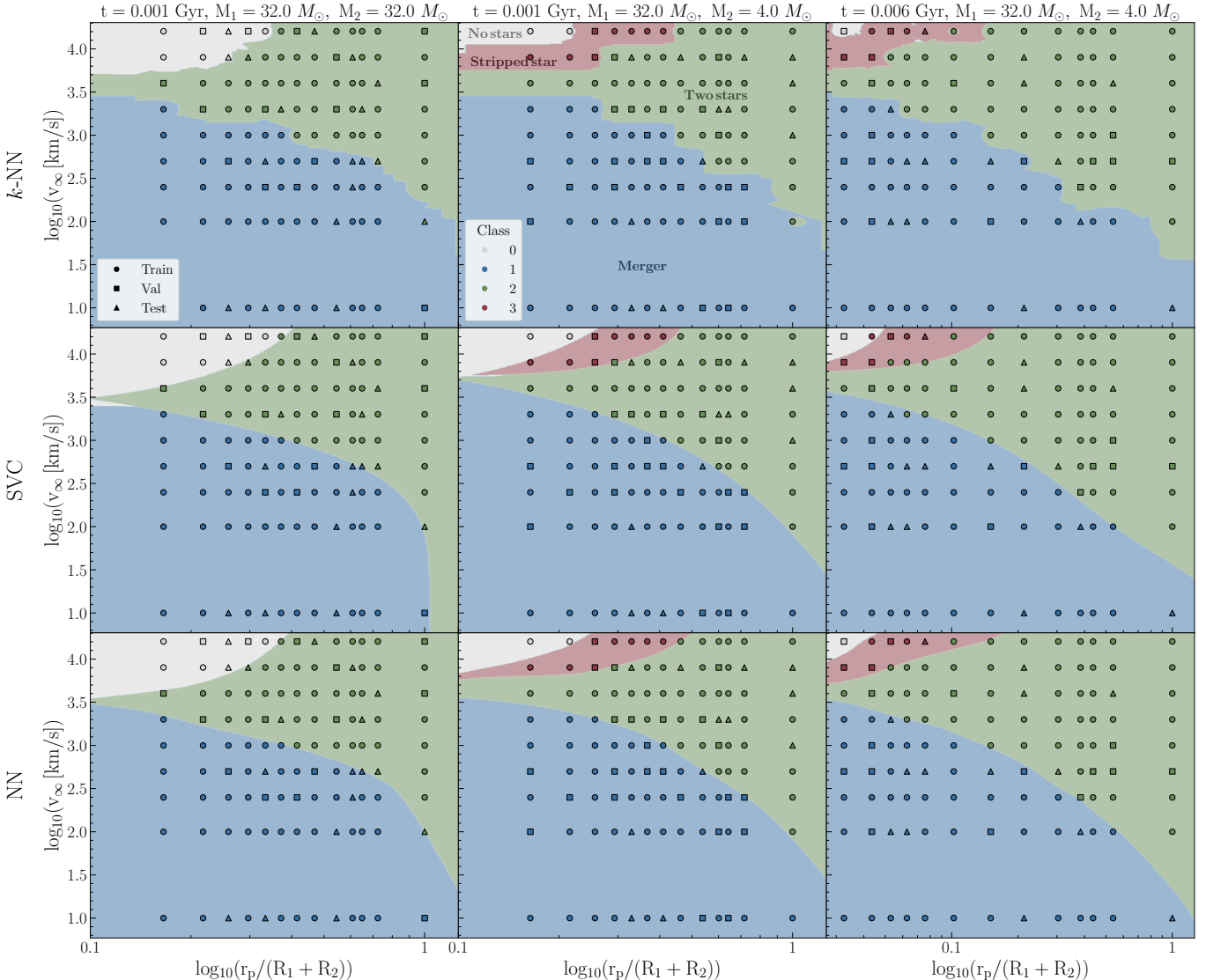


Figure 3. Two dimensional examples of decision boundaries for the stellar collision outcome classification task as a function of pericenter distance (r_p) and speed at infinity (v_∞) for fixed age and stellar mass values. Each color indicates a different class, where 0 is a mutual destruction case, 1 is a merger, 2 a fly by, and 3 a stripped star. The different marker shapes indicate the training (circles), validation (squares), and testing (triangles) datasets and are colored according to the ground truth. Classification predictions are shown as a background contour. Each column represents a different collision regime, where the first column is an equal mass collision, the middle panel is an unequal mass ratio collision, and the third panel is at the TAMS of the primary star. The x axis is normalized to standardize the scales across columns.

The median absolute errors for $M_{1,f}$ are comparable between the k -NN and SVR models. However, the same is not true for $M_{2,f}$, as the SVR predictions exhibit errors approximately three orders of magnitude larger. The superior performance of k -NN indicates that regression quantities in this input space are well-approximated by adjacent neighbors, and parametric methods such as SVRs struggle to capture it. Nevertheless, median relative errors for $M_{2,f}$ (in cases where the star survives) remain below 2% for the SVR.

4.3. Neural Network

As in Section 3.3, the NN used for the regression task is an MLP composed of three hidden layers, with 512, 256, and 128 neurons, each followed by a ReLU activation function and layer normalization. A key architectural feature is the application of a softmax function to the network outputs, which enforces mass conservation by requiring the three predicted mass fractions to be positive and sum to one.

The loss is defined as the MAE of the predictions. Because the predicted values correspond to the final

Table 3. Regression Hyperparameters

Parameter	Optimized Value	Hyperparameter Search Range
Epochs	2000	500 – 2000
Batch Size	64	64 – 512
Optimizer	AdamW	AdamW, sgd
Scheduler	CA-LR	CA-LR, RLRP
Learning Rate	0.0002	10^{-5} – 0.1
patience	...	10 – 120
factor	...	0.2 – 0.8
auxweight	0.31	0.05 – 1.0

NOTE—Hyperparameter optimization search for the regression task. Acronyms: stochastic gradient descent (sgd), AdamW optimizer (AdamW), Cosine Annealing Learning Rate scheduler (CA-LR), and Reduce Learning Rate on Plateau scheduler (RLRP).

fractional mass in each stellar component and unbound mass, the loss represents the error in the final predicted masses normalized by the total initial mass in the system. In addition, the contribution to the loss from the predicted unbound mass term is weighted in order to be less than or equal to the loss from the predicted masses. This is done to encourage the model to prioritize minimizing errors in the predicted stellar masses rather than the unbound mass. The value of this weight (`auxweight`) is treated as a hyperparameter and optimized during tuning.

We perform hyperparameter tuning as described in Section 3.3 and list the explored range in each parameter along with the optimal configuration in Table 3. For each hyperparameter configuration, the epoch with the lowest validation loss is selected to avoid overfitting. The optimized epoch value (2000) is at the edge of the explored range, but we confirmed that training converged. The model in the sweep with the lowest validation median absolute error in $M_{1,f}$ is selected as the best-performing model. Median-based metrics are adopted because they more accurately reflect the typical regression error and are less sensitive to outliers arising from misclassified points near decision boundaries. Furthermore, the errors in $M_{1,f}$ were chosen as our primary metric to select the best-performing model for two reasons: (1) in cases where only a single star survives, the final mass is always assigned to star 1, and (2) minimizing errors in $M_{1,f}$ effectively improves performance for the remaining predicted quantities due to the enforced mass conservation restriction. Following the same procedure as in Section 3.3, we conduct an additional sweep that varies the random seed to test for model stability. This yields the best-performing model with median absolute errors of $0.0047M_{\odot}$ for $M_{1,f}$ and 3.7×10^{-7} for $M_{2,f}$. Errors in $M_{2,f}$ are smaller than those in $M_{1,f}$ because $M_{2,f}$ is zero in a significant portion of the dataset (in cases of a stellar merger and mutual disruption), and

Table 4. Regression Performance Metrics

Method	Median Absolute Error [M_{\odot}]		Median Relative Error	
	$M_{1,f}$	$M_{2,f}$	$M_{1,f}$	$M_{2,f}$
k -NN	0.021	1e-05	0.0037	0.011
SVR	0.028	0.021	0.0045	0.015
NN [$\times 10^{-3}$]	4.67 ± 0.23 (best: 4.41)	0.00047 ± 0.00038 (best: 0.00037)	1.09 ± 0.05 (best: 1.05)	1.76 ± 0.15 (best: 1.51)

NOTE—Regression performance metrics for k -Nearest Neighbors (k -NN), support vector regression (SVR), and neural network (NN). We report the mean and standard deviation across ten runs with optimized hyperparameters and different random seeds. Fractional relative errors are only computed for cases where the star survives. Note that performance metrics for the NN are scaled by a factor of 10^{-3} .

the model accurately predicts these zero values. All regression performance metrics are listed in Table 4.

Figure 4 shows the predicted final stellar masses as functions of pericenter distance and relative velocity at infinity for a collision between two $32M_{\odot}$ stars at 1 Myr. The model predictions are shown as shaded contour maps, while training and validation samples are shown as scatter points colored by their ground-truth values. Testing points are colored according to the absolute errors of their predictions.

Qualitatively, despite the simplicity, the k -NN model captures the boundaries between different collision outcomes and exhibits relatively smooth predictions within each region. In contrast, the SVR suffers from non-physical features within each region, such as localized increases in mass loss at velocities between 10 and 100 km/s. The NN recovers the transition boundaries accurately and, like k -NN, reproduces characteristic features of equal-mass collisions, such as identical final masses when both survive (shown in light gray).

Quantitatively, the highest errors occur near transition boundaries, as expected. These errors are in fact misclassifications and are fundamentally different from regression errors for correctly classified data points. For example, errors in data points away from the transition boundaries tend to be smaller.

To characterize the error distributions across the entire test dataset, Figure 5 shows violin plots of the absolute and relative errors for all three methods. For predictions of $M_{1,f}$, k -NN and SVR exhibit similar absolute and relative error distributions, while the NN achieves a lower mean and median errors.

For $M_{2,f}$, the k -NN and NN error distributions show pronounced tails toward small absolute errors, corresponding to cases in which the final mass is correctly predicted to be close to zero (i.e., collisions where either only one star survives or both stars are destroyed). Although the SVR exhibits a larger median absolute error for $M_{2,f}$, its relative-error distribution indicates that, in

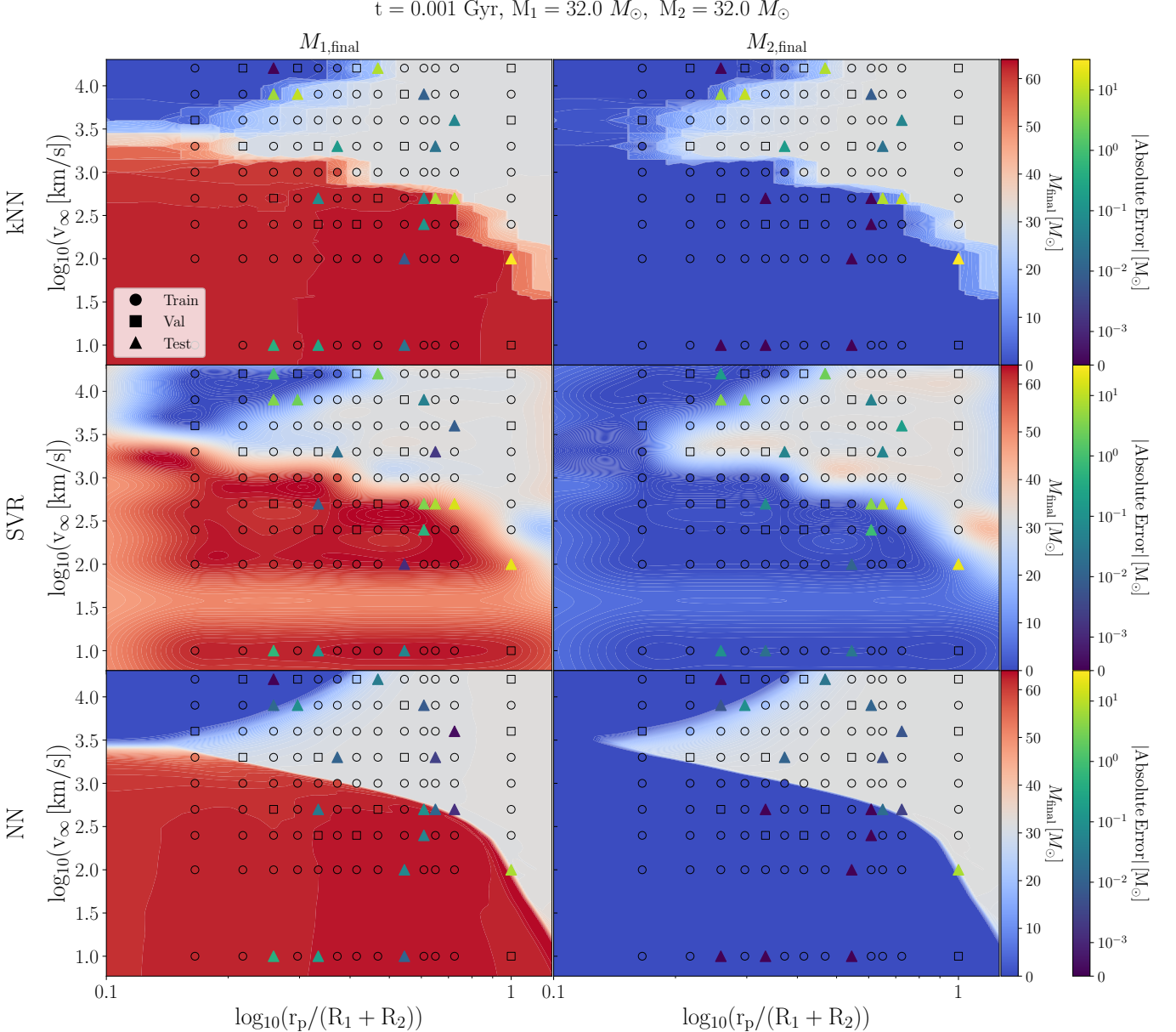


Figure 4. Examples of 2D regression maps for the final stellar masses as a function of pericenter distance (r_p) and relative velocity at infinity (v_∞). From top to bottom, the rows indicate predictions from k -Nearest Neighbors (k -NN), Support Vector Regression (SVR), and Neural Networks (NN). The first two columns show predicted final stellar masses in the color gradient, while the rightmost color shows the absolute error in the predictions for the test dataset. The different markers indicate points from the training (circles), validation (squares), and testing (triangles) datasets. The training and validation points are colored according to the ground truth.

cases where $M_{2,f}$ is non-zero and therefore relevant, the SVR performs comparably to k -NN. The NN achieves median and mean relative errors below 1% for both stellar masses. Overall, the error distributions shown in Figure 5, together with the performance metrics in Table 4, demonstrate that the NN achieves the lowest errors across all regression targets and is therefore the best-performing method.

5. MIXTURE OF EXPERTS

While training a classifier and a regressor separately yields high accuracies, here we investigate whether a shared architecture between the two tasks can further improve model performance. To this end, we draw inspiration from the Mixture of Experts (MoE) architecture (Jordan & Jacobs 1993), which is designed to handle complex data by training different “experts” on separate tasks. A gating mechanism, or router, determines which

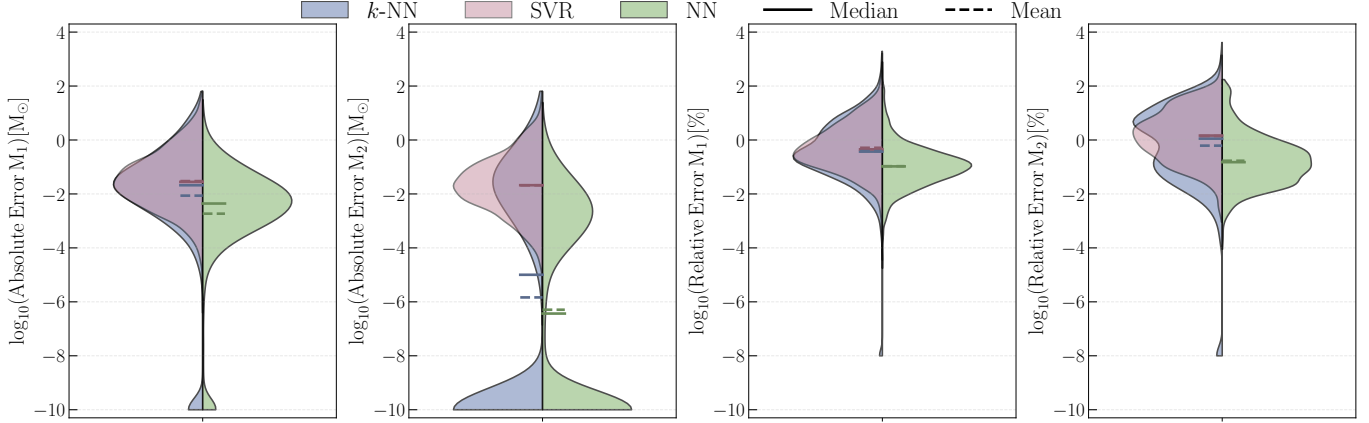


Figure 5. Absolute (left two panels) and relative (right two panels) error distribution in the predicted final stellar masses. Colors indicate the results from different algorithms. Colored solid (dashed) bars indicate the median (mean) of each distribution.

data each expert specializes in. Optimizing this gating mechanism is crucial for achieving a well-performing model.

In our approach, we leverage the classification predictions as a gating mechanism to route samples to specialized regression experts, each trained exclusively with data from one class. This design offers two key advantages. First, it enhances interpretability, as it is explicitly known which type of data should be routed to each expert, in contrast to an optimized gating mechanism where routing decisions are learned implicitly. Second, this architecture is motivated by the strong dependence of regression properties on collision outcomes. For instance, mutual destruction events will always result in both final masses being zero. By training individual experts on separate collision outcomes, we enable each model to specialize in distinct physical regimes instead of requiring one model to capture all regression patterns simultaneously.

The MoE architecture is shown in Figure 6. The five-dimensional input data is first passed through a shared backbone consisting of two fully-connected layers with dimensions 512 and 256, each followed by layer normalization and ReLU activation. The features are then fed into a classification head composed of one fully-connected layer (dimension 128) with layer normalization and ReLU activation, followed by a final layer that maps to four-dimensional logits corresponding to the collision outcome classes. The predicted class label is then used as a gating mechanism to route the data to its corresponding regression expert. Each expert has the same one-layer architecture as the classification head, but we apply a final linear layer that outputs the three predicted values followed by a softmax activation to ensure mass conservation.

When training a multitask NN such as our MoE architecture, the structure of the loss function is crucial to optimize task-specific metrics. As described in Sections 3.3 and 4.3, we use cross-entropy loss for the classifica-

Table 5. MoE Hyperparameters

Parameter	Optimized Value	Hyperparameter Search Range
Epoch	500	500 – 2000
Batch Size	128	64 – 512
Learning Rate	0.0004	10^{-5} – 0.1
Optimizer	AdamW	AdamW, sgd
Scheduler	CA-LR	CA-LR, RLRP
<code>patience</code>	...	5 – 80
<code>factor</code>	...	0.2 – 0.8
<code>auxweight</code>	0.77	0.05 – 1.0

NOTE—Hyperparameter optimization search for the regression task. Acronyms: stochastic gradient descent (`sgd`), AdamW optimizer (`AdamW`), Cosine Annealing Learning Rate scheduler (`CA-LR`), and Reduce Learning Rate on Plateau scheduler (`RLRP`).

tion task and MAE loss for the regression task. The regression loss is comprised of two terms, one for the predicted final mass fractions in each star, and another for the fraction of unbound mass. The weight for the unbound mass term is optimized during hyperparameter tuning (`auxweight`). To combine the task-specific losses into a joint loss, we use uncertainty-weighted loss (see Eq. 10 in Kendall et al. 2017) with the modification to the regularization term outlined in Liebel & Körner (2018), which weights each task-specific loss by a learnable parameter that is jointly optimized with the network weights. This eliminates the need for deciding the respective weights in the loss function from each task.

A Weights and Biases sweep is performed, with the explored hyperparameter ranges and optimized values listed in Table 5. The epoch with the lowest validation loss is chosen, as a low validation loss will correspond to high balanced accuracy and low absolute errors in the predicted mass fractions. We score models using the metric described in the Appendix C, which prioritizes classification performance while rewarding low regres-

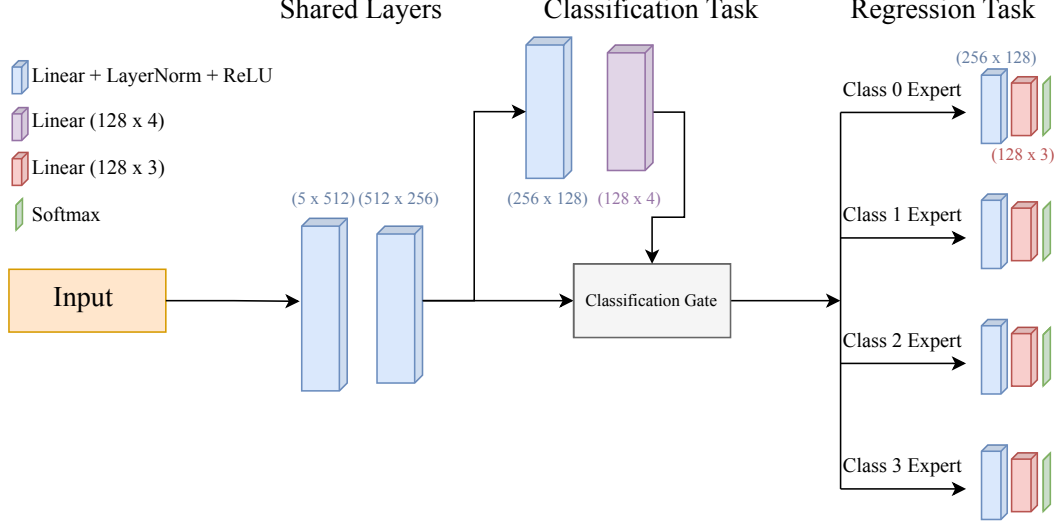


Figure 6. Diagram of our Mixture of Experts (MoE) Neural Network. The five-dimensional input data is passed through a shared backbone before being sent to a classification head. The classification labels are used as the gating mechanism to send data to its specialized expert according to its collision outcome class. The regression experts share the same NN structure as the classification heads, with an additional soft max activation function to ensure mass conservation.

sion errors above a defined threshold. As in the previous sections, we perform an additional sweep which includes different random seeds, arriving at a best-performing model with a balanced accuracy in the classification task of 98.5% and median absolute errors of $0.01M_{\odot}$ and $0.000004M_{\odot}$ in $M_{1,f}$ and $M_{2,f}$, respectively. Additional performance metrics are listed in Table 6. Note that some of the reported errors are smaller than the mass of a single SPH particle. However, they remain informative in this context, as they indicate the errors from the NN predictions.

Figure 7 shows the confusion matrix of the best-performing MoE model. The classification balanced accuracy, also listed in Table 6, is comparable to that of the SVR and NN models discussed in Sections 3.2 and 3.3, indicating that the gating mechanism is well-trained. This is particularly important because the accuracy of the regression predictions relies on the data being routed to the appropriate regression head.

Shown in Table 6 are the performance metrics for the regressed quantities, with the metrics from the individually trained NNs in Sections 3.3 and Sections 4.3 included for convenience. To visualize the differences in the error distributions between the individually trained NN and the MoE architecture, Figure 8 shows the distribution of absolute errors in the final mass predictions for different ground truth class labels. Across all labels and for both masses, the regression NN consistently has lower mean and median errors compared to the MoE.

For class 0 outcomes, both methods yield median and mean errors well below the minimum precision at which the data are physically meaningful. For label 1 data,

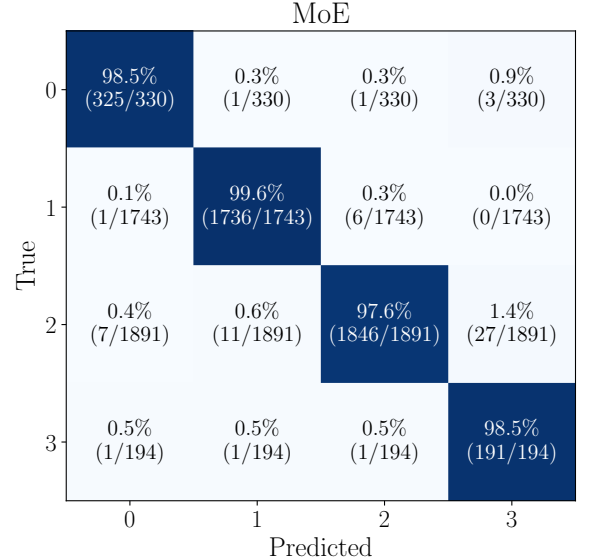


Figure 7. Confusion matrix for the testing data using Mixture of Experts (MoE). The accuracy and total number of samples in each class are shown.

the errors in the final mass of the merger product $M_{1,f}$ (always assigned to star 1) are comparable between the two methods, as are the errors for $M_{1,f}$ in the label 3 case. For both final masses in label 2 cases, the separately trained NN outperforms the MoE predictions. The effectiveness of the routing gates at reducing high absolute errors outliers can be seen in the error distributions for $M_{1,f}$ in case 0 and $M_{2,f}$ in case 3, where the NN

Table 6. MoE and Separate NN Performance Metrics

Model	Accuracy [%]	Balanced Accuracy [%]	Median Absolute Error [M_{\odot}]		Median Relative Error	
			$M_{1,f} [\times 10^{-3}]$	$M_{2,f} [\times 10^{-3}]$	$M_{1,f} [\times 10^{-3}]$	$M_{2,f} [\times 10^{-3}]$
MoE	98.5 ± 0.1 (best: 98.6)	98.2 ± 0.2 (best: 98.5)	12.5 ± 1.5 (best: 10.4)	0.01 ± 0.01 (best: 0.004)	3.1 ± 0.3 (best: 2.7)	8.4 ± 1.7 (best: 7.5)
Separate NN	98.5 ± 0.4 (best: 98.6)	97.9 ± 0.2 (best: 98.4)	4.67 ± 0.23 (best: 4.41)	0.00047 ± 0.00038 (best: 0.00037)	1.09 ± 0.05 (best: 1.05)	1.76 ± 0.15 (best: 1.51)

NOTE—Classification and regression performance metrics for Mixture-of-Experts (MoE). We report the mean and standard deviation across ten runs with optimized hyperparameters and different random seeds. Relative errors are only computed for cases where the star survives. The metrics for the classification and regression neural networks described in Sections 3.3 and 4.3, respectively, are included for convenience. Note that regression performance metrics are scaled by a factor of 10^{-3} .

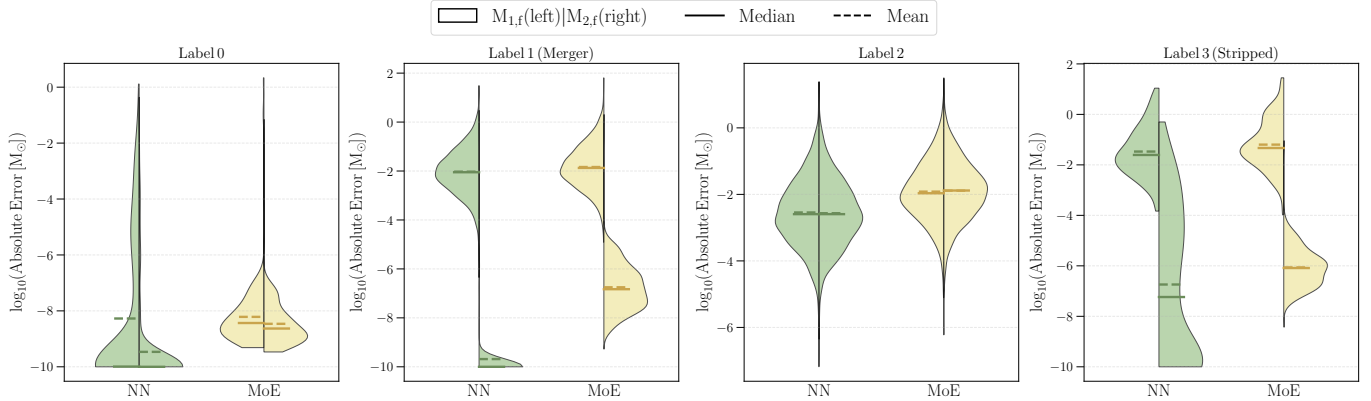


Figure 8. Distribution of absolute errors in the final predicted masses using the neural network (NN) described in Section 4.3 and the Mixture of Experts (MoE) described in Section 5. Each panel shows the distribution of absolute errors for the final masses of star 1 on the left and star 2 on the right of the violin plot, for data with a specific ground truth classification label. Small errors are rounded to 10^{-10} . Solid (dashed) lines show median (mean) values of the raw distribution.

has a tail towards higher errors, while the MoE exhibits a more constrained distribution at lower errors.

The observed differences in the error distributions are due to the structure of the loss function, and its effectiveness at balancing the relative importance of each task. In the individually trained regression NN, the loss function includes only terms directly related to the regression quantities. In contrast, the MoE loss function combines terms from both the classification and regression tasks adaptively throughout training. Details of the MoE loss function during training are provided in Appendix B. Future studies will explore alternative MoE architectures and loss functions to improve predictive accuracy.

6. A NEW SOFTWARE TOOL FOR STELLAR COLLISIONS

Building on the models developed in the previous sections, we introduce `collAIder`, a tool designed to predict stellar interaction outcomes and remnant properties. This tool leverages ML models to provide rapid predictions for interactions between two MS stars across

a wide range in masses, pericenter distances, and velocities. While prediction accuracy is the highest within the parameter space sampled by the SPH grid, the tool has been designed to generalize beyond the direct physical collision regime, extending into the tidal capture and fly-by limits. Extrapolation beyond the sampled space can yield inaccurate results, which we explore in Section 7.

The largest pericenter distance sampled in our grid is the sum of the individual stellar radii. However, stellar interactions at larger radii can yield interesting results as well. For example, close passages between stars can induce stellar oscillations that dissipate orbital energy (e.g., Lee & Ostriker 1986; Press & Teukolsky 1977). If the tidal perturbation is strong enough, on the order of the orbital energy, the two stars can then form a bound system. This is known as “tidal capture,” first invoked to explain the close X-ray binaries observed in globular clusters (Fabian et al. 1975). At distances larger than the capture radius, the stars will simply pass by each other without forming a bound system or colliding, i.e., a simple fly-by.

The pipeline begins by identifying whether the given initial properties of the interaction are in the collision, tidal capture, or fly-by regimes. To do this, for a given stellar interaction, if $r_p > R_1 + R_2$, we calculate the energy dissipated by tides in the following way.

Press & Teukolsky (1977) and Lee & Ostriker (1986) derived the expression for energy dissipation from tides as

$$\Delta E_1 = \left(\frac{GM_1^2}{R_1} \right) \left(\frac{M_2}{M_1} \right)^2 \sum_{l=2}^{\infty} \left(\frac{R_1}{r_p} \right)^{2l+2} T_l(\eta) \quad (4)$$

where $l = 2$ is the quadrupole term, $l = 3$ the octupole term, etc., and $T_l(\eta)$ is a dimensionless function of

$$\eta = \left(\frac{M_1}{M_1 + M_2} \right)^{\frac{1}{2}} \left(\frac{r_p}{R_1} \right)^{\frac{3}{2}} \quad (5)$$

Most of the orbital energy is transferred through the quadrupole and octupole perturbations, so we limit our approximations to only those terms. For simplicity, and to enable the use of pre-determined fits, we assign each star an effective polytropic index for the purpose of computing $T_l(\eta)$ values: for stars with $M < 0.4M_\odot$ we use $n = 1.5$ (appropriate for fully convective low-mass MS stars), while for stars with $M > 0.8M_\odot$ we use $n = 3$ (representing a more centrally condensed structure). This mapping is adopted for computational convenience. A more self-consistent approach would compute $T_l(\eta)$ for each stellar model from linear oscillation calculations, for example using GYRE (Townsend & Teitler 2013; Sun et al. 2023), but that is beyond the scope of the present work. For stars with masses between 0.4 and $0.8M_\odot$, we calculate the energy from tides for both polytropic indices at each given mass, and interpolate the final approximate values as

$$E_{\text{approx}} = \frac{E_3(M_\star - 0.4M_\odot) + E_{1.5}(0.8M_\odot - M_\star)}{0.4M_\odot} \quad (6)$$

where E_3 and $E_{1.5}$ are the energy losses from tidal dissipation for $n = 3$ and $n = 1.5$ for a given mass M_\star , respectively. The values for $T_l(\eta)$ are taken from the fits in Portegies Zwart & Meinen (1993). We do not apply these fits for data with $\eta > 10$ and instead assume energy dissipation through tidal interactions is negligible (since high η values correspond to pericenter distances in the fly-by regime).

Finally, to estimate stellar radii for any given mass, we interpolate from the two nearest stellar mass tracks provided by Posydon v2 (Andrews et al. 2025). More specifically, our tool includes an HDF5 file containing the single-star MESA hydrogen-MS evolution tracks, which finely sample initial stellar masses from 0.1 to $300M_\odot$. For a given stellar mass and age, we interpolate each radius to the target age. Then, we perform a second

interpolation between the two radii based on the target mass. This method allows us to accurately estimate stellar radii quickly, using MESA models that were generated with almost identical stellar evolution prescriptions to the ones in the SPH grid.

These single-star MESA models also enable us to determine whether a given star has evolved beyond the TAMS. For each star, we compare the central hydrogen abundances of the neighboring tracks in mass and age used for interpolation. We define the TAMS as the epoch where the central hydrogen abundance falls below 10^{-5} . We then take the minimum of the two TAMS ages and raise a `ValueError` if the user-provided age exceeds the TAMS by more than 10%. This step prevents extrapolation into evolutionary phases where the collision results will be very sensitive to stellar structure and which are not part of the current training data.

Finally, if the interaction is determined to be in the direct collision regime ($r_p \leq R_1 + R_2$), then the two ML models are used to predict the outcome and final masses. If the interaction is in the tidal capture limit, a merger with no mass loss is assumed (e.g., Benz & Hills 1987; Lai et al. 1993). Lastly, in the case of a fly-by both stellar masses are returned unchanged. A flowchart illustrating the decision process in `collAIder` is shown in Figure 9.

Given the marginal outperformance of the individually trained NNs over the MoE, we employ the former as the ML model to predict collision outcomes. As shown in the first panel of Figure 8, the regression model returns continuous values and therefore never predicts a final mass exactly equal to zero. Rather than applying a minimum mass cutoff for the remnant object—which makes assumptions about what is considered a collision product—we adjust the regression predictions based on the classification output to ensure consistency.

For example, when the classifier predicts a merger, the regression model may return a small (but nonzero) mass for star 2, alongside a correct prediction for the merger remnant. To address this discrepancy, we set $M_{2,f}$ exactly to zero and add its predicted mass to the ejected mass. This approach is valid because the NN was trained with the merger mass always assigned to $M_{1,f}$.

Consequently, the performance metrics change compared to those listed in Table 2 and Table 4. We report the adjusted performance metrics on the test dataset using `collAIder` in Table 7 and explore its performance at both interpolation and extrapolation in the section below. For the test dataset, we observe a slight decrease in accuracy and balanced accuracy for the classification task. This occurs because some inputs are classified as tidal captures or fly-bys (instead of direct collisions) due to slight differences between the stellar radii predicted by our MESA models and those from the Posydon v2 dataset. Nevertheless, the performance difference is negligible. For the regression task, errors remain compa-

CollAIder Flowchart

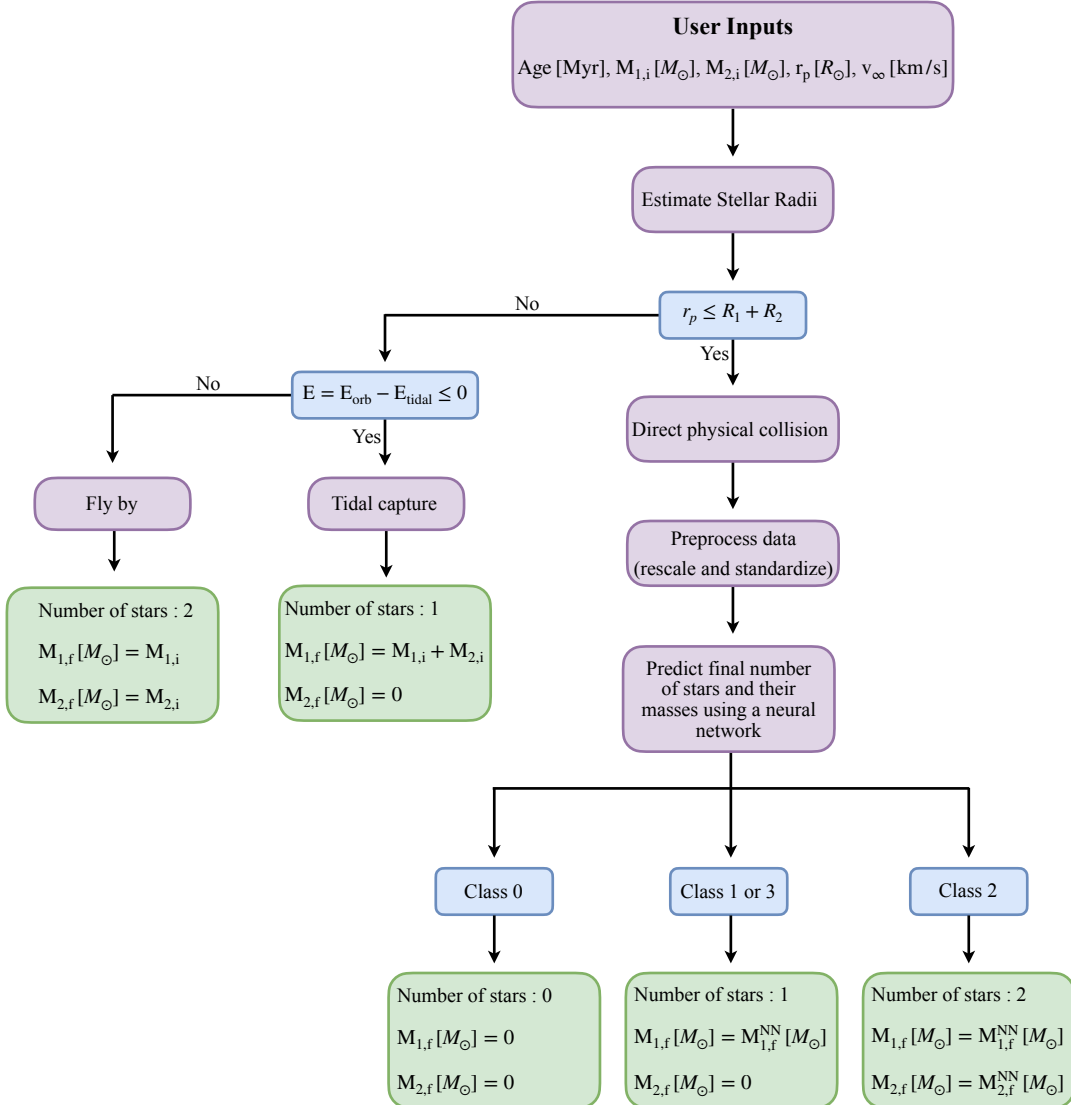


Figure 9. Flowchart illustrating the decision process in `collAIder`, described in Section 6. Blue boxes indicate decision points, while green boxes denote the final outputs of the software package. The neural network is only used when the input parameters correspond to a physical collision, and the regression outputs are adjusted based on the classification decisions. Masses with a NN superscript indicate predictions obtained using the neural network.

table. A median error of $0M_{\odot}$ for $M_{2,f}$ results from the added step of rounding $M_{2,f}$ to zero in cases of mergers or mutual destruction.

7. STRESS TESTS

The full parameter space for initial conditions is vast, and it extends past the values sampled in this study. To test the robustness of our NN models, we have performed additional SPH simulations both within the interpolation regime as well as for data outside of the sampled parameter space.

- **Interpolation:** For the interpolation dataset, we primarily focus on evaluating how the model generalizes for different initial masses. We perform SPH collisions involving 45 and $23M_{\odot}$ stars at 2.5 Myr, which is roughly halfway through the main sequence lifetime of the $45M_{\odot}$ star. We ran collisions at pericenter distances enclosing $0, 0.4, 0.8$, and 1 of the total stellar mass, and at velocities $(10, 500, 2000, 8000)$ km/s.

Table 7. `collAIder` Performance Metrics

Dataset	Accuracy [%]	Balanced Accuracy [%]	Median Absolute Error [M_{\odot}]		Median Relative Error	
			$M_{1,f}$	$M_{2,f}$	$M_{1,f}$	$M_{2,f}$
Testing	98.2	98.2	0.0043	0.0	0.0011	0.0014
Interpolation	100	100	0.091	0.0	0.0022	0.0036
TAMS	94.9	89.4	0.0086	0.0	0.0041	0.0044
Extrapolation	84.4	78.6	1.53	0.0	0.015	0.033

NOTE—Performance metrics using the `collAIder` package on the datasets described in Section 7. The second and third columns show accuracy and balanced accuracy for the classification task. The fourth and fifth columns show the median absolute errors in the final mass predictions for stars 1 and 2, respectively. The sixth and seventh columns show the median relative errors in the final mass predictions for the cases where the respective star survives.

- **TAMS Set:** We constructed a grid at 562 Myr, near the TAMS for a $2M_{\odot}$ star (~ 600 Myr), following the same sampling techniques for the secondary masses, velocities, and pericenter distances as the base TAMS grid. Although this grid is almost identical to the existing $2M_{\odot}$ TAMS grid, we aim to test how well the model adapts to collisions of stars near the TAMS.
- **Extrapolation Set:** Crucially, we wanted to assert how reliable the models are for out-of-distribution data. Because our SPH models rely on MESA profiles, we have limited this testing data set to two stellar masses, 75 and $90M_{\odot}$. Note that they are both outside of the range of stellar masses explored in this study. We perform collisions between the $75M_{\odot}$ and $90M_{\odot}$ stars at 0.07 and 3.3 Myr, roughly at the ZAMS of the $75M_{\odot}$ star and at the TAMS of the $90M_{\odot}$. This serves the purpose of testing whether the algorithm has learned the importance of stellar structure variations across time. We perform collisions with the same pericenter and velocities values as in the interpolation dataset.

The predictions were computed using `collAIder` to obtain performance metrics representative of what a user would experience. These metrics are summarized in Table 7. For the classification task, the extrapolation set shows the largest decrease in performance with a balanced accuracy of 78.6%. This is expected since both the interpolation and TAMS datasets lie within the range of explored masses and ages. For the regression task, median absolute errors remain low for most datasets, with the notable exception of the extrapolation dataset, which has a median absolute error of $1.53M_{\odot}$ for $M_{1,f}$. However, the corresponding relative error (excluding mutual destruction cases) is only 1.5%, indicating good accuracy given that the initial masses are both at least $75M_{\odot}$. Across all datasets, relative errors in the final mass predictions are below 1.5% and 3.3% for $M_{1,f}$ and $M_{2,f}$, respectively.

In addition, we performed a targeted stress test motivated by a case from the forthcoming work of Parmerlee et al. 2026 in which `collAIder` predicts a small net mass gain by the more massive star during a grazing encounter. Such outcomes are uncommon but do occur in the SPH dataset. In grazing envelope–envelope interactions, some shocked fluid is brought to low speeds in the center of mass system and can later be re-accreted: if more material originating from star 2 falls back onto star 1 than mass from star 1 becomes unbound, star 1 can experience a small net mass gain. Because our regression model predicts the partition of the bound mass among the two survivors while enforcing overall mass conservation, it naturally permits this behavior rather than imposing mass loss for each star.

Our specific test involves the collision at age 0.79 Gyr with $(M_{1,i}, M_{2,i}) = (1.593, 1.128) M_{\odot}$, $r_p = 0.568 R_{\odot}$, and $v_{\infty} = 584 \text{ km s}^{-1}$. The SPH simulation yields a two-star outcome with $(M_{1,f}, M_{2,f}) = (1.599, 1.104) M_{\odot}$. In this case star 1 gains $0.006 M_{\odot}$ (0.4%) while the system as a whole loses $0.017 M_{\odot}$ (0.6%) to unbound ejecta. The `collAIder` prediction for the same initial conditions correctly captures the sign of the effect ($M_{1,f} > M_{1,i}$), and although it overpredicts the accreted mass, the predicted $M_{1,f} = 1.63 M_{\odot}$ remains within 2% of the SPH value. This demonstrates that the model can reproduce these rare events at a level consistent with the expected accuracy of the regression task.

8. DISCUSSION & CONCLUSIONS

In this work we have presented a new set of 27,720 SPH simulations of stellar collisions spanning a wide range of ages, masses, relative velocities, and pericenter distances. This comprehensive dataset is used to train machine learning models to predict not only the outcome of the interaction but also the final masses of the remnant stars. In this regime, there are three possible classification labels, 0, 1, 2, and 3. The first three intuitively indicate the number of remnant stars: 0 denotes mutual destruction events, 1 denotes mergers, and 2 mild collisions. Label 3 indicates stripped star cases, where a highly energetic event (at high relative speeds

and moderately small pericenter distances) completely destroys one star and partially strips the other one. Although one star remains in this case, it is its own class label since the hydrodynamic evolution of the collision is very different. For the regression task, the model is trained to predict the final fractional mass in each star and unbound material. The NN is set up in a way that ensures mass conservation. We compare the classification and regression performance of three ML algorithms (k -NN, SVM, and NNs), finding:

- **Classification:** the SVM and NN have comparable performance, with balanced accuracies of 97.7% and 98.4%, respectively. This is unsurprising, as SVMs are well suited for multi-class classification. Furthermore, most of the misclassified data points lie near the decision boundaries, as expected.
- **Regression:** the NN outperforms all other methods, with a median absolute error in stellar masses of $0.00441M_{\odot}$ for $M_{1,f}$ and $3.7 \times 10^{-7}M_{\odot}$ for $M_{2,f}$. The corresponding relative errors are 0.11% and 0.15%. As is the case for the classification task, most errors lie along areas near the decision boundaries, where small deviations in initial conditions produce large changes in the final masses of the stars.

We also investigated whether a MoE architecture, which consists of initial shared layers followed by four separate regression experts, each trained on data corresponding to predicted classification labels, would outperform the separately-trained NNs. We find that the MoE has comparable balanced accuracy for the classification task and slightly larger errors for regression. Nevertheless, the gating mechanism is well-trained and the performance of the MoE model remains comparable to that of the individually trained NNs. Future studies will investigate different MoE architectures to improve performance further.

Finally, we present the package `collAIder`, which uses the trained ML models to predict stellar collision outcomes and remnant properties. The package, outlined in Section 6, classifies stellar encounters in the direct physical collision, tidal capture, and fly by regime, returning predictions for a wide range of dynamical properties. Its performance is tested on interpolation, extrapolation, and near-TAMS cases. The model struggles the most with the extrapolation dataset, yielding a balanced accuracy of 78.6% and median relative errors of 1.5% and 3.3% in the final predicted masses of stars 1 and 2, respectively.

Although it is already quite extensive, the SPH grid used here to train the ML models encompasses a limited range of sampled stellar models and collision parameters. Thus, performance will inevitably decrease for data

beyond the sampled ranges. Nevertheless, the extrapolation tests outlined in Section 7 already show satisfactory performance for collisions involving MS stars with metallicity of $0.01Z_{\odot}$.

The `collAIder` pipeline approximates stellar radii to estimate whether the encounter will be in the direct physical collision regime (in which case the ML model is used for inference), the tidal capture regime (in which case a merger with no mass loss is assumed) or a distant fly by. These stellar radii are interpolated using the `Posydon v2 MESA` tracks (Andrews et al. 2025). While these tracks sample stellar masses and ages very finely, interpolation is still needed to infer radii at arbitrary user inputs. Uncertainties in these interpolated values introduce small errors in stellar radii which can, in edge cases, cause misclassifications in the nature of the encounter.

Furthermore, predictions are limited to MS stars with metallicity $Z = 0.01Z_{\odot}$. Future work will expand into other metallicities as well as incorporate collisions involving giant stars and compact objects.

This work showcases the potential impact and application of ML algorithms trained on large datasets. Such NN models can dramatically reduce computational costs and deliver physically-consistent results almost immediately. A particularly impactful application lies in N -body simulations, where no mass loss is often assumed for stellar collisions. Incorporating ML models into large-scale N -body frameworks will enable more realistic treatment of stellar collisions, with crucial implications for understanding collision remnants and their properties, including blue stragglers, BHs in the upper-mass gap, and the transient signals that might accompany these collisions. Forthcoming work (Parmerlee et al. 2026, in prep.) performs initial tests of the NN models presented in this paper by implementing them into semi-analytical models of the Milky Way’s Galactic center.

9. ACKNOWLEDGEMENTS

We thank Ugur Demir, Nabeel Rehembtulla, Ved Shah, and Philipp Srivastava for useful discussions. This work was supported by NSF Grant AST-2511543 to F.A.R. and T.S. at Northwestern University. Support for E.G.P. was provided by the NSF Graduate Research Fellowship Program under Grant DGE-2234667. S.C.R. is grateful for support from the Lindheimer Fellowship. F.K. and C.E.O. acknowledge support from a CIERA Postdoctoral Fellowship. T.C.P. was supported in part by NSF Grants AST-2149425 and AST-2446392. We gratefully acknowledge the support of the NSF-Simons AI-Institute for the Sky (SkAI) via grants NSF AST-2421845 and Simons Foundation MPS-AI-00010513. This work used Bridges-2 at Pittsburgh Supercomputing Center through allocation PHY-240311 from the Advanced Cyberinfrastructure Coordination Ecosystem: Services & Support (ACCESS) program,

which is supported by NSF Grants 2138259, 2138286, 2138307, 2137603, and 2138296. This research was also supported in part through the computational resources and staff contributions provided for the Quest high-performance computing facility at Northwestern Uni-

versity, which is jointly supported by the Office of the Provost, the Office for Research, and Northwestern University Information Technology. AF and SC also acknowledge the support of the Aspen Center for PHYics, funded by the NSF Grant PHY-2210452, where some of this work was initiated.

REFERENCES

Agarap, A. F. 2018, arXiv e-prints, arXiv:1803.08375, doi: [10.48550/arXiv.1803.08375](https://doi.org/10.48550/arXiv.1803.08375)

Agrawal, P., Hurley, J., Stevenson, S., Szécsi, D., & Flynn, C. 2020, MNRAS, 497, 4549, doi: [10.1093/mnras/staa2264](https://doi.org/10.1093/mnras/staa2264)

Amaro Seoane, P. 2023, ApJ, 947, 8, doi: [10.3847/1538-4357/ach8b9](https://doi.org/10.3847/1538-4357/ach8b9)

—. 2025, arXiv e-prints, arXiv:2509.12352, doi: [10.48550/arXiv.2509.12352](https://doi.org/10.48550/arXiv.2509.12352)

Andrews, J. J., Bavera, S. S., Briel, M., et al. 2025, ApJS, 281, 3, doi: [10.3847/1538-4365/adfb78](https://doi.org/10.3847/1538-4365/adfb78)

Asplund, M., Grevesse, N., Sauval, A. J., & Scott, P. 2009, ARA&A, 47, 481, doi: [10.1146/annurev.astro.46.060407.145222](https://doi.org/10.1146/annurev.astro.46.060407.145222)

Balberg, S., Sari, R., & Loeb, A. 2013, MNRAS, 434, L26, doi: [10.1093/mnrasl/slt071](https://doi.org/10.1093/mnrasl/slt071)

Balberg, S., & Yassur, G. 2023, ApJ, 952, 149, doi: [10.3847/1538-4357/acdd73](https://doi.org/10.3847/1538-4357/acdd73)

Baumgardt, H., & Hilker, M. 2018, MNRAS, 478, 1520, doi: [10.1093/mnras/sty1057](https://doi.org/10.1093/mnras/sty1057)

Benz, W., & Hills, J. G. 1987, ApJ, 323, 614, doi: [10.1086/165857](https://doi.org/10.1086/165857)

Brutman, Y., Steinberg, E., & Balberg, S. 2024, ApJL, 974, L22, doi: [10.3847/2041-8213/ad808f](https://doi.org/10.3847/2041-8213/ad808f)

Cambioni, S., Asphaug, E., Emsenhuber, A., et al. 2019, ApJ, 875, 40, doi: [10.3847/1538-4357/ab0e8a](https://doi.org/10.3847/1538-4357/ab0e8a)

Cambioni, S., Jacobson, S. A., Emsenhuber, A., et al. 2021, PSJ, 2, 93, doi: [10.3847/PSJ/abf0ad](https://doi.org/10.3847/PSJ/abf0ad)

Choi, J., Dotter, A., Conroy, C., et al. 2016, ApJ, 823, 102, doi: [10.3847/0004-637X/823/2/102](https://doi.org/10.3847/0004-637X/823/2/102)

Cortes, C., & Vapnik, V. N. 1995, Machine Learning, 20, 273. <https://api.semanticscholar.org/CorpusID:52874011>

Cover, T., & Hart, P. 1967, IEEE Transactions on Information Theory, 13, 21, doi: [10.1109/TIT.1967.1053964](https://doi.org/10.1109/TIT.1967.1053964)

Dale, J. E., Davies, M. B., Church, R. P., & Freitag, M. 2009, MNRAS, 393, 1016, doi: [10.1111/j.1365-2966.2008.14254.x](https://doi.org/10.1111/j.1365-2966.2008.14254.x)

Emsenhuber, A., Cambioni, S., Asphaug, E., et al. 2020, ApJ, 891, 6, doi: [10.3847/1538-4357/ab6de5](https://doi.org/10.3847/1538-4357/ab6de5)

Fabian, A. C., Pringle, J. E., & Rees, M. J. 1975, MNRAS, 172, 15, doi: [10.1093/mnras/172.1.15P](https://doi.org/10.1093/mnras/172.1.15P)

Fragos, T., Andrews, J. J., Bavera, S. S., et al. 2023, ApJS, 264, 45, doi: [10.3847/1538-4365/ac90c1](https://doi.org/10.3847/1538-4365/ac90c1)

Freitag, M., & Benz, W. 2005, MNRAS, 358, 1133, doi: [10.1111/j.1365-2966.2005.08770.x](https://doi.org/10.1111/j.1365-2966.2005.08770.x)

Freitag, M., Dale, J. E., Church, R. P., & Davies, M. B. 2007, Proceedings of the International Astronomical Union, 3, 211–214, doi: [10.1017/S1743921308017675](https://doi.org/10.1017/S1743921308017675)

Fukushima, K. 1969, IEEE Transactions on Systems Science and Cybernetics, 5, 322, doi: [10.1109/TSSC.1969.300225](https://doi.org/10.1109/TSSC.1969.300225)

Gaburov, E., Lombardi, Jr., J. C., & Portegies Zwart, S. 2010, MNRAS, 402, 105, doi: [10.1111/j.1365-2966.2009.15900.x](https://doi.org/10.1111/j.1365-2966.2009.15900.x)

Genzel, R., Eisenhauer, F., & Gillessen, S. 2010, Reviews of Modern Physics, 82, 3121, doi: [10.1103/RevModPhys.82.3121](https://doi.org/10.1103/RevModPhys.82.3121)

Gibson, C., Kiroğlu, F., Lombardi, J. C., Jr., et al. 2024, arXiv e-prints, arXiv:2410.02146, doi: [10.48550/arXiv.2410.02146](https://doi.org/10.48550/arXiv.2410.02146)

Glebbeek, E., Pols, O. R., & Hurley, J. R. 2008, A&A, 488, 1007, doi: [10.1051/0004-6361:200809930](https://doi.org/10.1051/0004-6361:200809930)

Glorot, X., Bordes, A., & Bengio, Y. 2011, in Proceedings of the Fourteenth International Conference on Artificial Intelligence and Statistics, 315–323

González Prieto, E., Weatherford, N. C., Fragione, G., Kremer, K., & Rasio, F. A. 2024, ApJ, 969, 29, doi: [10.3847/1538-4357/ad43d6](https://doi.org/10.3847/1538-4357/ad43d6)

Gürkan, M. A., Fregeau, J. M., & Rasio, F. A. 2006, ApJL, 640, L39, doi: [10.1086/503295](https://doi.org/10.1086/503295)

Harris, W. E. 2010, arXiv e-prints, arXiv:1012.3224, doi: [10.48550/arXiv.1012.3224](https://doi.org/10.48550/arXiv.1012.3224)

Hornik, K., Stinchcombe, M., & White, H. 1989, Neural Networks, 2, 359, doi: [10.1016/0893-6080\(89\)90020-8](https://doi.org/10.1016/0893-6080(89)90020-8)

Hu, B. X., & Loeb, A. 2024, A&A, 689, A23, doi: [10.1051/0004-6361/202450308](https://doi.org/10.1051/0004-6361/202450308)

Hurley, J. R., Pols, O. R., Aarseth, S. J., & Tout, C. A. 2005, MNRAS, 363, 293, doi: [10.1111/j.1365-2966.2005.09448.x](https://doi.org/10.1111/j.1365-2966.2005.09448.x)

Hurley, J. R., Tout, C. A., Aarseth, S. J., & Pols, O. R. 2001, MNRAS, 323, 630, doi: [10.1046/j.1365-8711.2001.04220.x](https://doi.org/10.1046/j.1365-8711.2001.04220.x)

Hwang, J., Lombardi, Jr., J. C., Rasio, F. A., & Kalogera, V. 2015, *ApJ*, 806, 135, doi: [10.1088/0004-637X/806/1/135](https://doi.org/10.1088/0004-637X/806/1/135)

Ivanova, N., Justham, S., Avendano Nandez, J. L., & Lombardi, J. C. 2013, *Science*, 339, 433, doi: [10.1126/science.1225540](https://doi.org/10.1126/science.1225540)

Jermyn, A. S., Bauer, E. B., Schwab, J., et al. 2023, *ApJS*, 265, 15, doi: [10.3847/1538-4365/aca8d](https://doi.org/10.3847/1538-4365/aca8d)

Jordan, M., & Jacobs, R. 1993, in *Proceedings of 1993 International Conference on Neural Networks (IJCNN-93-Nagoya, Japan)*, Vol. 2, 1339–1344 vol.2, doi: [10.1109/IJCNN.1993.716791](https://doi.org/10.1109/IJCNN.1993.716791)

Kendall, A., Gal, Y., & Cipolla, R. 2017, arXiv e-prints, arXiv:1705.07115, doi: [10.48550/arXiv.1705.07115](https://doi.org/10.48550/arXiv.1705.07115)

Kirilov, A., Calderón, D., Pejcha, O., & Duffell, P. C. 2025, *ApJL*, 994, L41, doi: [10.3847/2041-8213/aelae7](https://doi.org/10.3847/2041-8213/aelae7)

Kiroğlu, F., Kremer, K., & Rasio, F. A. 2025, *ApJL*, 994, L37, doi: [10.3847/2041-8213/aeleeb](https://doi.org/10.3847/2041-8213/aeleeb)

Kiroğlu, F., Lombardi, J. C., Kremer, K., et al. 2023, *ApJ*, 948, 89, doi: [10.3847/1538-4357/acc24c](https://doi.org/10.3847/1538-4357/acc24c)

Kremer, K., Lombardi, J. C., Lu, W., Piro, A. L., & Rasio, F. A. 2022, *ApJ*, 933, 203, doi: [10.3847/1538-4357/ac714f](https://doi.org/10.3847/1538-4357/ac714f)

Kremer, K., Lu, W., Rodriguez, C. L., Lachat, M., & Rasio, F. A. 2019, *ApJ*, 881, 75, doi: [10.3847/1538-4357/ab2e0c](https://doi.org/10.3847/1538-4357/ab2e0c)

Kremer, K., Spera, M., Becker, D., et al. 2020, *ApJ*, 903, 45, doi: [10.3847/1538-4357/abb945](https://doi.org/10.3847/1538-4357/abb945)

Lai, D., Rasio, F. A., & Shapiro, S. L. 1993, *ApJ*, 412, 593, doi: [10.1086/172946](https://doi.org/10.1086/172946)

LeCun, Y., Bengio, Y., & Hinton, G. 2015, *Nature*, 521, 436, doi: [10.1038/nature14539](https://doi.org/10.1038/nature14539)

Lee, H. M., & Ostriker, J. P. 1986, *ApJ*, 310, 176, doi: [10.1086/164674](https://doi.org/10.1086/164674)

Lei Ba, J., Kiros, J. R., & Hinton, G. E. 2016, arXiv e-prints, arXiv:1607.06450, doi: [10.48550/arXiv.1607.06450](https://doi.org/10.48550/arXiv.1607.06450)

Leonard, P. J. T. 1989, *AJ*, 98, 217, doi: [10.1086/115138](https://doi.org/10.1086/115138)

Liebel, L., & Körner, M. 2018, arXiv e-prints, arXiv:1805.06334, doi: [10.48550/arXiv.1805.06334](https://doi.org/10.48550/arXiv.1805.06334)

Lombardi, Jr., J. C., Proulx, Z. F., Dooley, K. L., et al. 2006, *ApJ*, 640, 441, doi: [10.1086/499938](https://doi.org/10.1086/499938)

Lombardi, Jr., J. C., Rasio, F. A., & Shapiro, S. L. 1996, *ApJ*, 468, 797, doi: [10.1086/177736](https://doi.org/10.1086/177736)

Lopez, Jr., M., Batta, A., Ramirez-Ruiz, E., Martinez, I., & Samsing, J. 2019, *ApJ*, 877, 56, doi: [10.3847/1538-4357/ab1842](https://doi.org/10.3847/1538-4357/ab1842)

Loshchilov, I., & Hutter, F. 2017, arXiv e-prints, arXiv:1711.05101, doi: [10.48550/arXiv.1711.05101](https://doi.org/10.48550/arXiv.1711.05101)

Maas, A. L., Hannun, A. Y., & Ng, A. Y. 2013, in *Proc. ICML Workshop on Deep Learning for Audio, Speech and Language Processing*

MacLeod, M., Macias, P., Ramirez-Ruiz, E., et al. 2017, *ApJ*, 835, 282, doi: [10.3847/1538-4357/835/2/282](https://doi.org/10.3847/1538-4357/835/2/282)

McCulloch, W. S., & Pitts, W. 1943, *Bull. Math. Biol.*, 5, 115, doi: [10.1007/BF02478259](https://doi.org/10.1007/BF02478259)

Metzger, B. D., & Pejcha, O. 2017, *MNRAS*, 471, 3200, doi: [10.1093/mnras/stx1768](https://doi.org/10.1093/mnras/stx1768)

Monaghan, J. J. 1992, *ARA&A*, 30, 543, doi: [10.1146/annurev.aa.30.090192.002551](https://doi.org/10.1146/annurev.aa.30.090192.002551)

Nandez, J. L. A., Ivanova, N., & Lombardi, Jr., J. C. 2014, *ApJ*, 786, 39, doi: [10.1088/0004-637X/786/1/39](https://doi.org/10.1088/0004-637X/786/1/39)

Neights, E., Burns, E., Fryer, C. L., et al. 2026, *MNRAS*, 545, staf2019, doi: [10.1093/mnras/staf2019](https://doi.org/10.1093/mnras/staf2019)

O'Connor, B., Gill, R., DeLaunay, J., et al. 2025, *ApJL*, 994, L17, doi: [10.3847/2041-8213/ae1741](https://doi.org/10.3847/2041-8213/ae1741)

Paszke, A., Gross, S., Massa, F., et al. 2019, arXiv e-prints, arXiv:1912.01703, doi: [10.48550/arXiv.1912.01703](https://doi.org/10.48550/arXiv.1912.01703)

Paxton, B., Bildsten, L., Dotter, A., et al. 2011, *ApJS*, 192, 3, doi: [10.1088/0067-0049/192/1/3](https://doi.org/10.1088/0067-0049/192/1/3)

Paxton, B., Cantiello, M., Arras, P., et al. 2013, *ApJS*, 208, 4, doi: [10.1088/0067-0049/208/1/4](https://doi.org/10.1088/0067-0049/208/1/4)

Paxton, B., Marchant, P., Schwab, J., et al. 2015, *ApJS*, 220, 15, doi: [10.1088/0067-0049/220/1/15](https://doi.org/10.1088/0067-0049/220/1/15)

Paxton, B., Schwab, J., Bauer, E. B., et al. 2018, *ApJS*, 234, 34, doi: [10.3847/1538-4365/aaa5a8](https://doi.org/10.3847/1538-4365/aaa5a8)

Paxton, B., Smolec, R., Schwab, J., et al. 2019, *ApJS*, 243, 10, doi: [10.3847/1538-4365/ab2241](https://doi.org/10.3847/1538-4365/ab2241)

Payne, A. V., Shappee, B. J., Hinkle, J. T., et al. 2021, *ApJ*, 910, 125, doi: [10.3847/1538-4357/abe38d](https://doi.org/10.3847/1538-4357/abe38d)

Pedregosa, F., Varoquaux, G., Gramfort, A., et al. 2011, *Journal of Machine Learning Research*, 12, 2825

Peng, Z.-k., Gao, H., & Zhang, X.-F. 2025, *ApJ*, 995, 58, doi: [10.3847/1538-4357/ae1583](https://doi.org/10.3847/1538-4357/ae1583)

Perets, H. B., Li, Z., Lombardi, Jr., J. C., & Milcarek, Jr., S. R. 2016, *ApJ*, 823, 113, doi: [10.3847/0004-637X/823/2/113](https://doi.org/10.3847/0004-637X/823/2/113)

Planck Collaboration, Ade, P. A. R., Aghanim, N., et al. 2016, *A&A*, 594, A13, doi: [10.1051/0004-6361/201525830](https://doi.org/10.1051/0004-6361/201525830)

Portegies Zwart, S. F., Baumgardt, H., Hut, P., Makino, J., & McMillan, S. L. W. 2004, *Nature*, 428, 724, doi: [10.1038/nature02448](https://doi.org/10.1038/nature02448)

Portegies Zwart, S. F., & Meinen, A. T. 1993, *A&A*, 280, 174

Press, W. H., & Teukolsky, S. A. 1977, *ApJ*, 213, 183, doi: [10.1086/155143](https://doi.org/10.1086/155143)

Pryor, C., & Meylan, G. 1993, in *Astronomical Society of the Pacific Conference Series*, Vol. 50, *Structure and Dynamics of Globular Clusters*, ed. S. G. Djorgovski & G. Meylan, 357

Rasio, F. A. 1991, PhD thesis, Cornell University, New York

Rauch, K. P. 1999, *ApJ*, 514, 725, doi: [10.1086/306953](https://doi.org/10.1086/306953)

Rose, S. C., Lombardi, Jr., J. C., González Prieto, E., Kiroğlu, F., & Rasio, F. A. 2025, arXiv e-prints, arXiv:2511.01811, doi: [10.48550/arXiv.2511.01811](https://doi.org/10.48550/arXiv.2511.01811)

Rose, S. C., & Mockler, B. 2025, ApJL, 985, L40, doi: [10.3847/2041-8213/add266](https://doi.org/10.3847/2041-8213/add266)

Rose, S. C., Naoz, S., Sari, R., & Linial, I. 2023, arXiv e-prints, arXiv:2304.10569, doi: [10.48550/arXiv.2304.10569](https://doi.org/10.48550/arXiv.2304.10569)

Ryu, T., Amaro Seoane, P., Taylor, A. M., & Ohlmann, S. T. 2024, MNRAS, 528, 6193, doi: [10.1093/mnras/stae396](https://doi.org/10.1093/mnras/stae396)

Ryu, T., Perna, R., & Wang, Y.-H. 2022, MNRAS, 516, 2204, doi: [10.1093/mnras/stac2316](https://doi.org/10.1093/mnras/stac2316)

Sanders, R. H. 1970, ApJ, 162, 791, doi: [10.1086/150711](https://doi.org/10.1086/150711)

Shara, M. M. 2002, in Astronomical Society of the Pacific Conference Series, Vol. 263, Stellar Collisions, Mergers and their Consequences, ed. M. M. Shara, 1

Sills, A., Karakas, A., & Lattanzio, J. 2009, ApJ, 692, 1411, doi: [10.1088/0004-637X/692/2/1411](https://doi.org/10.1088/0004-637X/692/2/1411)

Snoek, J., Larochelle, H., & Adams, R. P. 2012, arXiv e-prints, arXiv:1206.2944, doi: [10.48550/arXiv.1206.2944](https://doi.org/10.48550/arXiv.1206.2944)

Spitzer, Jr., L., & Saslaw, W. C. 1966, ApJ, 143, 400, doi: [10.1086/148523](https://doi.org/10.1086/148523)

Sun, M., Townsend, R. H. D., & Guo, Z. 2023, ApJ, 945, 43, doi: [10.3847/1538-4357/acb33a](https://doi.org/10.3847/1538-4357/acb33a)

Townsend, R. H. D., & Teitler, S. A. 2013, MNRAS, 435, 3406, doi: [10.1093/mnras/stt1533](https://doi.org/10.1093/mnras/stt1533)

van der Merwe, C. J. T., Mohamed, S. S., José, J., Shara, M., & Kamiński, T. 2024, MNRAS, 534, 3637, doi: [10.1093/mnras/stae2329](https://doi.org/10.1093/mnras/stae2329)

van der Merwe, C. J. T., Mohamed, S. S., José, J., Shara, M. M., & Kamiński, T. 2025, MNRAS, 538, 1384, doi: [10.1093/mnras/staf328](https://doi.org/10.1093/mnras/staf328)

Wang, Y.-H., Perna, R., & Armitage, P. J. 2021, MNRAS, 503, 6005, doi: [10.1093/mnras/stab802](https://doi.org/10.1093/mnras/stab802)

Weinberger, R., Springel, V., & Pakmor, R. 2020, ApJS, 248, 32, doi: [10.3847/1538-4365/ab908c](https://doi.org/10.3847/1538-4365/ab908c)

Wendland, H. 1995, Advances in Computational Mathematics, 4, 389, doi: [10.1007/BF02123482](https://doi.org/10.1007/BF02123482)

Xin, C., Haiman, Z., Perna, R., Wang, Y., & Ryu, T. 2024, ApJ, 961, 149, doi: [10.3847/1538-4357/ad11d3](https://doi.org/10.3847/1538-4357/ad11d3)

APPENDIX

A. SVR GRIDSEARCH

In this section, we detail the grid search performed for the regression task using the support-vector regression (SVR) module in `ScikitLearn`. The grid search is performed for each regressed quantity separately, as summarized in Table 8. Three separate kernels were explored: radial basis function (`rbf`), polynomial, and sigmoid. A more limited exploration of the polynomial kernel was followed, since a single model can take several hours to train. The hyperparameter search ranges were chosen according to computational resources and to maximize exploration of the parameter space. For all quantities except the degree we searched over logarithmically-spaced values. The `C` parameter acts as a regularizer that controls the complexity of the model, with large values imposing stronger penalties and leading to more complex models. The parameter `gamma` determines the influence of individual training points and ϵ defines the width of the tube within which no penalty is assigned to errors. Following an initial coarse grid search, we conducted a refined search around smaller epsilon values using the optimized values found for the kernel, `C`, and `gamma`. The final optimized values are listed in Table 8.

Table 8. SVR Hyperparameter Grid Search Ranges

Quantity	Kernel	C	gamma	ϵ	Degree
Initial Coarse Grid Search					
$q_{1,f}$	<code>rbf</code>	0.1 – 100	0.01 – 10	0.001 – 0.1	—
$q_{1,f}$	Polynomial	0.1 – 10	0.01 – 1	0.01 – 0.1	2 – 3
$q_{1,f}$	Sigmoid	0.1 – 1000	0.01 – 10	0.0001 – 0.1	—
$q_{2,f}$	<code>rbf</code>	0.1 – 100	0.01 – 10	0.001 – 0.1	—
$q_{2,f}$	Polynomial	0.1 – 10	0.01 – 1	0.001 – 0.1	2 – 3
$q_{2,f}$	Sigmoid	0.1 – 1000	0.01 – 10	0.0001 – 0.1	—
$q_{u,f}$	<code>rbf</code>	0.1 – 100	0.01 – 10	0.001 – 0.1	—
$q_{u,f}$	Polynomial	0.1 – 10	0.01 – 1	0.001 – 0.1	2 – 3
$q_{u,f}$	Sigmoid	0.1 – 1000	0.01 – 10	0.0001 – 0.1	—
Refined Fine Grid Search					
All	<code>rbf</code>	1	10, 50	0.00001 – 0.001	—
Optimized Values					
All	<code>rbf</code>	1	10	0.00001	—

NOTE—Support Vector Regression (SVR) hyperparameter search for the final fractional mass in star 1 ($q_{1,f}$), star 2 ($q_{2,f}$), and unbound mass ($q_{u,f}$). A search was conducted across three kernels, the radial basis function (`rbf`), polynomial, and sigmoid.

B. MOE LOSS FUNCTION

The challenge of any multitask architecture is optimizing performance across all tasks. In this work, we have used uncertainty-weighted loss (see Eq. 10 in [Kendall et al. 2017](#)) with the modification to the regularization term outlined in [Liebel & Körner \(2018\)](#). This method weights the loss of each task by learnable parameters that are optimized with the network weights. In the left panel of Figure 10 we show the respective loss functions for the classification and regression tasks, alongside the overall loss of the model during the training. The figure shows both training and validation losses, illustrating that the model begins to overfit after approximately epoch 107 (kept as the best model), shown by the increase in the validation loss. The monotonic decrease of both task-specific loss functions demonstrates that the uncertainty-weighted approach is successfully balancing optimization across both tasks. The evolution of the learned weight parameters is shown in the right panel, with the optimal classification and regression uncertainty weights found to be 0.36 and 0.26, respectively.

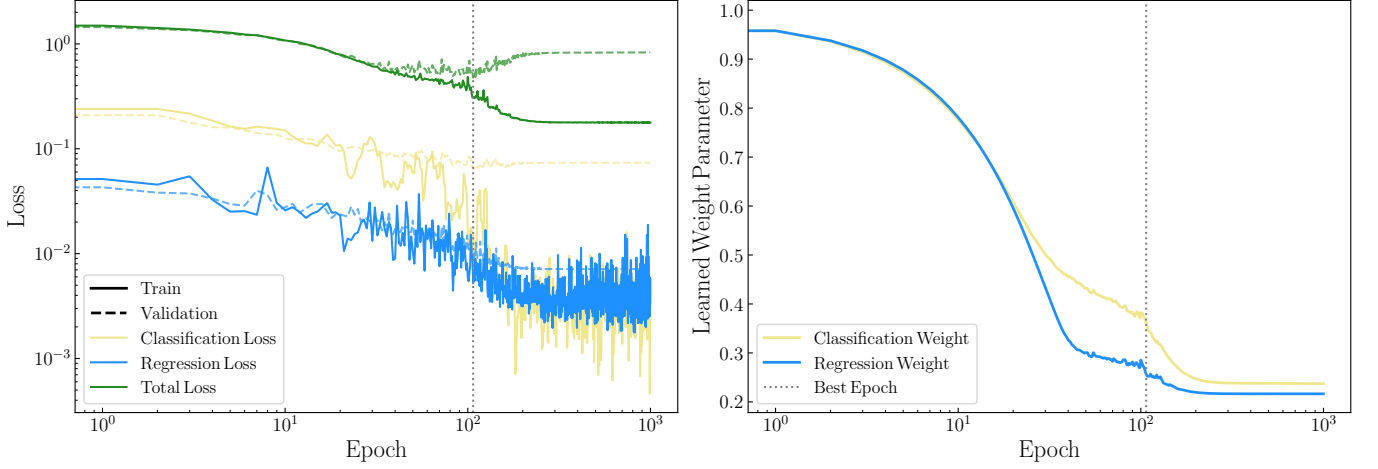


Figure 10. Training (Validation) loss functions for the classification and regression tasks shown in solid (dashed) yellow and blue, respectively. The total loss function is shown in green, obtained using uncertainty-weighted loss (Kendall et al. 2017, Eq. 10). The classification loss function is smoothed with a moving average of size 5 for visualization purposes. The dashed line indicates the epoch with the lowest validation loss.

C. MODEL SCORING

Because multitask NNs optimize multiple tasks simultaneously, a metric tailored to the specific science case is needed to evaluate model performance. We score the MoE models using

$$\text{Score} = \alpha'(1 - \text{BA}) + \beta' \text{MedAE}_1^* + \eta' \text{MedAE}_2^* \quad (\text{C1})$$

where BA is balanced accuracy and $\text{MedAE}_i^* = (\text{MedAE}_i - \text{MedAE}_{i,\min}) / (\text{MedAE}_{i,\max} - \text{MedAE}_{i,\min})$ are the min-max normalized median absolute errors in the predicted masses where $i = 1, 2$ indicate stars 1 and 2. The prefactors that weight each component are set to

$$(\alpha', \beta', \eta') = \begin{cases} (\alpha + \beta + \eta, 0, 0) & \text{if } \text{MedAE}_1, \text{MedAE}_2 < 0.005 \\ (\alpha, \beta + \eta, 0) & \text{if } \text{MedAE}_2 < 0.005 \\ (\alpha, 0, \eta + \beta) & \text{if } \text{MedAE}_1 < 0.005 \\ (\alpha, \beta, \eta) & \text{otherwise} \end{cases} \quad (\text{C2})$$

where $\alpha = 0.8$, and $\beta = \eta = 0.1$. The value of α is large to prioritize classification performance. Furthermore, we include a threshold of $0.005M_\odot$ for MedAE, below which we do not reward regression performance. This avoids rewarding improvement past an absolute error of $0.005M_\odot$, since that is negligible at the sampled masses. The model with the lowest score is selected as the best performing model. Note that this metric is particularly suited for the application of this tool and other scientific goals might require a different metric to identify the best model.